RING dimerisation drives higher-order organisation of SINA/SIAH E3 ubiquitin ligases

Franck Coste, Aanchal Mishra, Catherine Chapuis, Lucija Mance, Zofia Pukalo, Nicolas Bigot, Stéphane Goffinont, Virginie Gaudon, Norbert Garnier, Ibtissam Talhaoui, et al.

RING dimerisation drives higher-order organisation of SINA/SIAH E3 ubiquitin ligases

Franck Coste[1,✉], **Aanchal Mishra**[1,2], **Catherine Chapuis**[3], **Lucija Mance**[1,2], **Zofia Pukało**[1], **Nicolas Bigot**[3], **Stéphane Goffinont**[1], **Virginie Gaudon**[1], **Norbert Garnier**[1,4], **Ibtissam Talhaoui**[1], **Bertrand Castaing**[1,2], **Sebastien Huet**[3,✉], **Marcin J. Suskiewicz**[1,2,✉]

[1] Centre de Biophysique Moléculaire (CBM), UPR 4301, CNRS, Orléans, France
[2] École Doctorale « Santé, Science Biologique & Chimie du Vivant » (ED549), Université d'Orléans, Orléans, France
[3] Univ Rennes, CNRS, IGDR (Institut de génétique et développement de Rennes) - UMR 6290, BIOSIT (Biologie, Santé, Innovation Technologique) - UAR 3480, US_S 018, F35000 Rennes
[4] Pôle physique, Université d'Orléans, Orléans, France
✉ Correspondence: Franck Coste (franck.coste@cnrs-orleans.fr), Sébastien Huet (sebastien.huet@univ-rennes.fr), and Marcin J. Suskiewicz (marcin.suskiewicz@cnrs-orleans.fr)

RING-type E3 ubiquitin ligases promote ubiquitylation by stabilising an active complex between a ubiquitin-loaded E2-conjugating enzyme and a protein substrate. To fulfil this function, the E3 ubiquitin ligase SIAH1 and other SINA/SIAH-subfamily RING-type E3 ligases employ an N-terminal catalytic RING domain and a C-terminal substrate-binding domain (SBD), separated by two zinc fingers. Here, we present the first crystal structure of the RING domain of human SIAH1, together with an adjacent zinc finger, revealing a potential RING dimer, which was validated in solution using static light scattering. RING dimerisation contributes to the E3 ligase activity of SIAH1 both *in vitro* and in cells. Moreover, as the RING domain is the second element, after the SBD, to independently favour homodimerisation within SINA/SIAH E3 ligases, we propose that alternating RING:RING and SBD:SBD interactions organise multiple copies of a SINA/SIAH protein into a higher-order homomultimer. In line with this hypothesis, fluorescently-tagged full-length human SIAH1, human SIAH2, and fruit fly SINA show cytoplasmic clusters in human cells, whereas their distribution becomes more diffuse when RING dimerisation is disabled. The wild-type (WT) form of SIAH1, but not its RING dimerisation mutant, colocalises with aggregated synphilin-1A under proteasomal inhibition, suggesting that SIAH1 multimerisation might contribute to its reported preference for aggregated or multimeric substrates.

Introduction

Ubiquitylation, also called ubiquitination, is a post-translational modification (PTM) that regulates various aspects of protein function and is particularly important for targeting proteins for proteasomal degradation [1]. E3 ligases play a key role in determining the substrate specificity of this process, typically by recognising exposed motifs, referred to as 'degrons', on substrate proteins [2]. For some proteins, it has been possible to develop small molecules that artificially induce their recruitment to an E3 ligase, triggering their rapid ubiquitylation and degradation [3,4]. This pharmacological strategy, termed targeted protein degradation, presents an alternative to small-molecule inhibitors for selective inactivation of cellular proteins in fundamental biological research and in therapy [5–7].

The largest family among known E3 ubiquitin ligases, with more than 600 predicted members in human cells, are RING-type E3 ubiquitin ligases [8]. This family is defined by the presence of the Really Interesting New Gene (RING) domain, whose core comprises around 50 amino-acid residues and coordinates two zinc atoms. By employing diverse substrate-binding domains, RING-type E3 ligases deliver specific protein substrates to a ubiquitin-loaded E2 conjugating enzyme (ubiquitin~E2), in which ubiquitin is covalently bound to E2 through a reactive thioester bond. In addition to their roles as substrate adaptors, RING-type E3 ligases use their RING domain to stabilise the active, 'closed', conformation of the ubiquitin~E2 molecule, which would otherwise be flexible and thus inhibited [9–13]. Through this mechanism, the RING domain accelerates the discharge of ubiquitin from E2 onto a lysine residue in the recruited substrate.

Although many monomeric RING domains are known, RING homo- and heterodimerisation – ranging from transient to stable – is a recurrent feature observed in some RING-type E3 ligase subfamilies [8,14,15]. The dimerisation mediated by the RING domain can contribute to the organisation of RING-type E3 ligases into higher-order assemblies and sometimes aids in stabilising the closed conformation of ubiquitin~E2. Through the latter mechanism, RING dimerisation can contribute to the catalytic activity of ubiquitin E3 ligases.

The Seven IN Absentia (SINA)/Seven In Absentia Homologue (SIAH) ligases constitute one of the most highly conserved subfamilies of RING-type E3 ligases, with orthologues found across various kingdoms of life, from plants to humans [16–18]. SINA and SIAH proteins comprise a variable flexible region followed by four conserved domains: the N-terminal RING domain, two further zinc-finger domains (ZnF1 and ZnF2), and the C-terminal substrate-binding domains (SBD) (**Figure 1A**). The SBD – which is known to form a stable, high-affinity homodimer [18] – recognises specific degrons in substrates. For SIAH1, these degrons typically contain the core VXP sequence, where X is any amino acid [19–22].

SIAH1 and SIAH2 are important players in mammals at an organismal level, as indicated by the severe growth retardation and spermatogenesis failure of SIAH1 knockout mice [23] and the extremely early lethality (hours after birth) of the double SIAH1 and SIAH2 knockout mice [24]. By targeting specific proteins for degradation, human SIAH proteins contribute to a number of cellular processes, including cellular signalling – especially Rat Sarcoma Virus (RAS) and hypoxia pathways – and DNA-damage response, and as such they are investigated as potential targets for anti-cancer therapy [25]. Moreover, SIAH1 has been shown to ubiquitylate synphilin-1 and α-synuclein, components of Lewy bodies in Parkinson's patients [26].

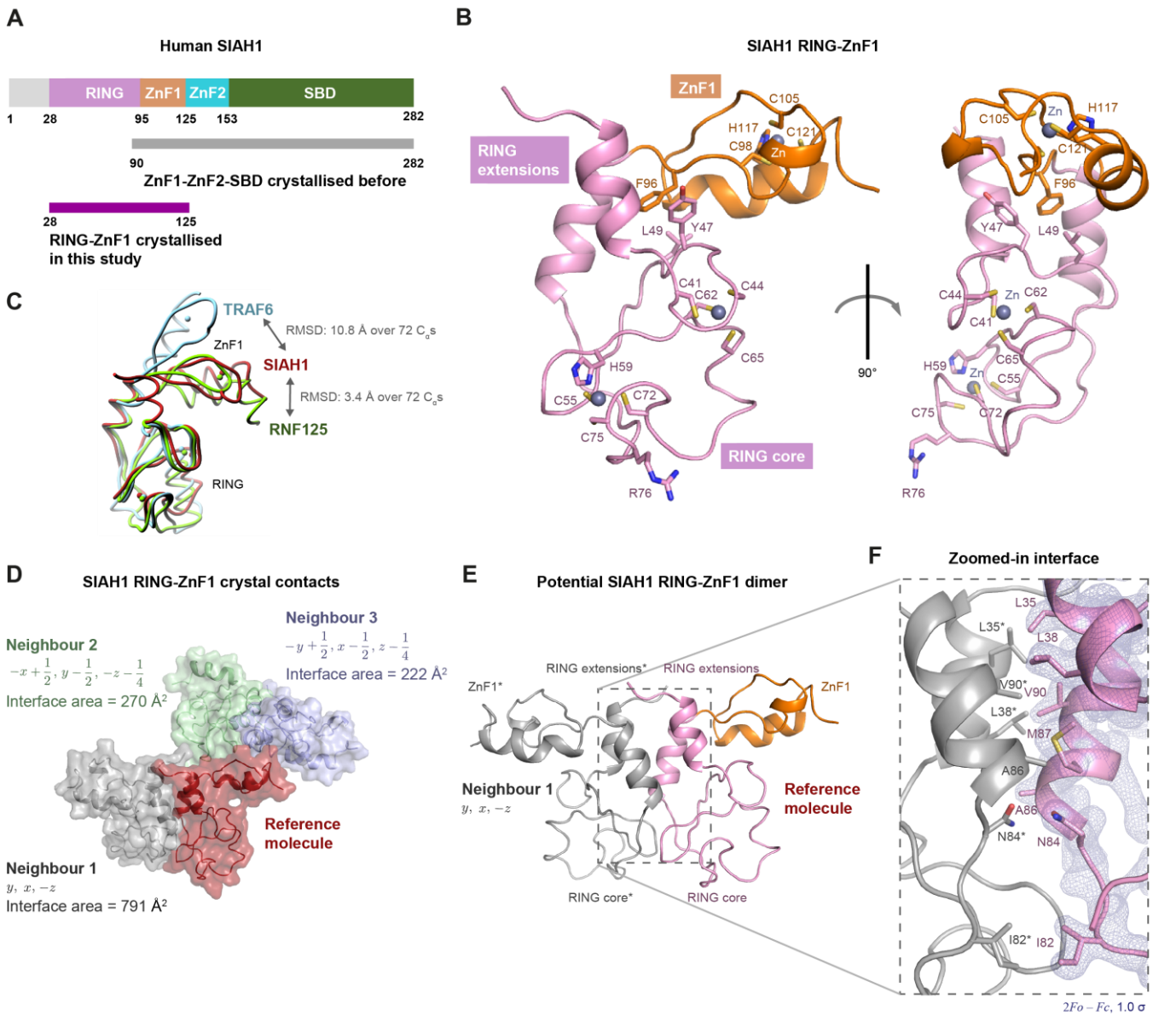

Figure 1 | Crystal structure of the RING-ZnF1 fragment of human SIAH1. (A) Domain architecture of human SIAH1. Residues 1-27 are predicted to be intrinsically disordered. The fragments crystallised before and in this study are indicated underneath. **(B)** A ribbon diagram of the crystal structure of the RING-ZnF1 fragment of human SIAH1 coloured according to the domain composition presented in panel A, with the RING domain together with its extensions in pink and the ZnF1 domain in orange. Selected amino-acid sidechains are shown as sticks and zinc atoms as green spheres. **(C)** Wire diagrams of crystal structures of RING-ZnF1 fragments of SIAH1, RNF125, and TRAF6, showing different relative orientations of RING and ZnF1 domains. Protein Data Bank entries used: 5VNZ (TRAF6) and 5DKA (RNF125). See the main text for references. RMSD values for the structural alignments of a monomer of SIAH1 and either TRAF6 or RNF125 over the indicated numbers of C_α atoms (C_αs) are provided. **(D)**Three distinct major crystal contacts observed between molecules from different asymmetric units in the SIAH1 RING-ZnF1 crystal lattice. A molecule considered as a reference (red) and its three neighbours related by indicated symmetry operations (grey, green, and blue) are shown in cartoon and transparent surface representation. The surface area of the interface between each neighbour and the reference molecule is provided. **(E)** A ribbon diagram of a potential dimer observed between molecules from neighbouring asymmetric units within the crystal lattice of the RING-ZnF1 structure of SIAH1. One subunit is coloured according to domain composition (like in panel A, with the extended RING domain in pink and ZnF1 in orange), while the other is uniformly grey. Zinc atoms are not shown. Asterisks denote elements/domains of Neighbour 1. **(F)** A zoomed-in view of the dimer interface with key amino-acid sidechains shown as sticks and labelled. The interacting chains are coloured like in panel E. A fragment of the *2Fo – Fc* electron density map corresponding to interface residues from one of the interacting chains is shown as a semi-transparent mesh contoured at 1*σ*. The electron density for the opposing chain is identical but has been omitted for enhanced clarity. Asterisks denote residues of Neighbour 1. All structural figures were generated in PyMol, except for panel C, which was created in Chimera.

In addition to its physiological roles, SIAH1 emerged as an actor in targeted protein degradation when Słabicki et al. identified it as the E3 ligase responsible for the degradation of the ZBTB-family oncoprotein BCL6 upon treatment with a small-molecule drug candidate, BI-3802 [27]. Interestingly, unlike in more typical cases of targeted protein degradation, BI-3802 does not directly "glue" the substrate to the E3 ligase. Instead, it induces noncovalent polymerisation of BCL6 dimers into filaments, which show enhanced binding and ubiquitylation by SIAH1 compared to native, dimeric BCL6. It remains unclear, however, why SIAH1 preferentially targets the polymerised form of BCL6. The process has been suggested to depend on multivalent interactions [4], but this is difficult to reconcile with the currently accepted dimeric state of SIAH1.

Crystal structures of fragments of SIAH1 comprising ZnF1, ZnF2, and SBD domains or just ZnF2 and SBD have been solved, both without and with substrate-derived peptides [18,20,22,28–30]. A structure of the ZnF1-ZnF2-SBD fragment of SIAH2 is available as well (PDB **5H9M**, unpublished). In contrast, the structure of the RING domain of any SINA/SIAH subfamily member has not been experimentally determined to date.

Here, we present the structure of the RING-ZnF1 fragment of human SIAH1, thus completing the experimental structural characterisation of the key elements constituting SINA/SIAH proteins. Our analysis suggests that the RING domain in human SIAH1, and likely in all SINA/SIAH E3 ligases, undergoes dimerisation. The uncovered RING dimerisation propensity contributes to the E3 ligase activity of SIAH1 both *in vitro* and in cells. Furthermore, as SIAH1 contains two antipodal homodimerising domains, RING and SBD, we propose that alternating RING:RING and SBD:SBD contacts between multiple SIAH1 subunits lead to the formation of higher-order chain-like assemblies, which could serve to concentrate SIAH1 in specific subcellular areas. In line with this hypothesis, deleting either the RING or the SBD domain or disrupting RING dimerisation changes the localisation of SINA/SIAH proteins from clustered to more diffuse in cultured cells. Furthermore, mutating the RING dimerisation inteface impairs the colocalisation of SIAH1 with aggregated synphilin-1A. We hypothesise that multivalency of the SIAH1 assemblies afforded by its multimerisation properties could account for its apparent preference for multivalent substrates, including aggregated components of Lewy bodies and BI-3802-induced BCL6 polymers.

Results

Structure of the RING-ZnF1 fragment of SIAH1

Since SINA/SIAH proteins had been only partially characterised in terms of experimental structural biology, our goal was to address this gap, with a focus on the uncharacterised RING domain. We began with recombinant bacterial production of various human SIAH1 constructs harbouring a non-cleavable hexahistidine tag at the C terminus. Our attempts to produce polypeptides that encompass all four folded domains (full-length SIAH1 or its fragment lacking the first 27 amino-acid residues predicted to be disordered) were unsuccessful, as these proteins showed low expression in *Escherichia coli* and/or formed insoluble inclusion bodies. We therefore shifted our focus to shorter constructs that covered different SIAH1 portions, including the RING domain alone (residues 28-100, of which residues 28-95 correspond to the RING domain), RING and ZnF1 together (residues 28-125), or RING, ZnF1, and ZnF2 together (residues 28-157, where ZnF2 is predicted to stop at residue 153) (**Figure 1A**). The second construct stood out due to the high yield of soluble protein, allowing successful purification and crystallisation.

We resolved the structure of the RING-ZnF1 fragment of human SIAH1 in the $P4_32_12$ space group at a resolution of 1.9 Å (**Figure 1B**, **Table 1**). An AlphaFold 2 model of this fragment was used as a search model for molecular replacement. The crystal structure, comprising a single SIAH1 fragment per asymmetric unit, shows a classical RING domain fold, stabilised by two zinc atoms coordinated through a cross-braced arrangement of cysteine and histidine residues. The so-called 'linchpin' arginine residue, which typically contributes to ubiquitylation catalysis by stabilising the closed conformation of ubiquitin~E2 in RING-type E3 ligases [11], is present in its expected position directly after one of the zinc-coordinating cysteine residues (Arg76). The core RING domain is flanked by short α-helices upstream and downstream of the domain (referred to here as RING extensions), similarly to what has been observed in some other RING-type E3 ligase subfamilies [8,14,15].

Following the downstream α-helical RING extension, the sequence continues into ZnF1, a slightly atypical zinc finger in terms of spacing between zinc-coordinating residues. ZnF1 of SIAH1 has been resolved before as part of a ZnF1-ZnF2-SBD construct [18,20,22] and its conformation in our structure is indistinguishable from that determined previously (RMSD < 0.5 Å over all ZnF1 C_α atoms). Several residues (particularly Tyr47 and Leu49 from RING and Phe96 from a region between RING and ZnF1) engage in contacts between RING and ZnF1 to stabilise what appears to be a relatively fixed orientation of the two domains with respect to each other. This tandem RING-ZnF1 arrangement is reminiscent of certain other RING-type E3 ligases including TRAF6 [31] and RNF125 [32]. The relative orientation of RING and ZnF1 in our SIAH1 structure is closest to that observed for RNF125 (**Figure 1C**).

Potential RING dimerisation in the crystal

The presence of α-helical segments flanking the RING domain is typically associated with a dimerisation propensity, with two copies of these α-helices creating a four-helix bundle upon self-association [8,14,15]. Since our SIAH1 RING-ZnF1 crystals contained only a single molecule in the asymmetric unit, we analysed the crystallographic lattice in search of crystallographic neighbours that could correspond to a dimerisation partner. This analysis revealed three distinct extensive crystal contacts between individual SIAH1 RING-ZnF1 molecules within the lattice, of which one – between the reference molecule and a neighbour related by an $x, y, -z$ symmetry operator – is distinguished by a large interface surface area and a two-fold rotational symmetry (**Figure 1D**). This crystal contact – which notably involves the RING extensions on the two interacting molecules – likely reflects a solution homodimer.

As expected based on structures of other RING dimers, this potential interaction is stabilised primarily by the four-helix bundle formed by the α-helical RING extensions (**Figure 1E**), with hydrophobic residues Leu35 and Leu38 from the upstream α-helix and Met87 and Val90 from the downstream α-helix engaging in contacts with their crystallographic copies across the two-fold axis (**Figure 1F**). Additionally, the core RING domains also interact with each other – especially through Ile82 – resulting in a tight packing of the two copies across the entire length of the extended RING domain. All amino-acid sidechains contributing to this potential homodimerisation interface are well-resolved in the $2Fo - Fc$ electron density map. The ZnF1 domain is oriented away from this interface, with none of its residues directly participating in the proposed interaction.

Overall, this analysis reveals an interaction between SIAH1 RING-ZnF1 molecules from two neighbouring crystal

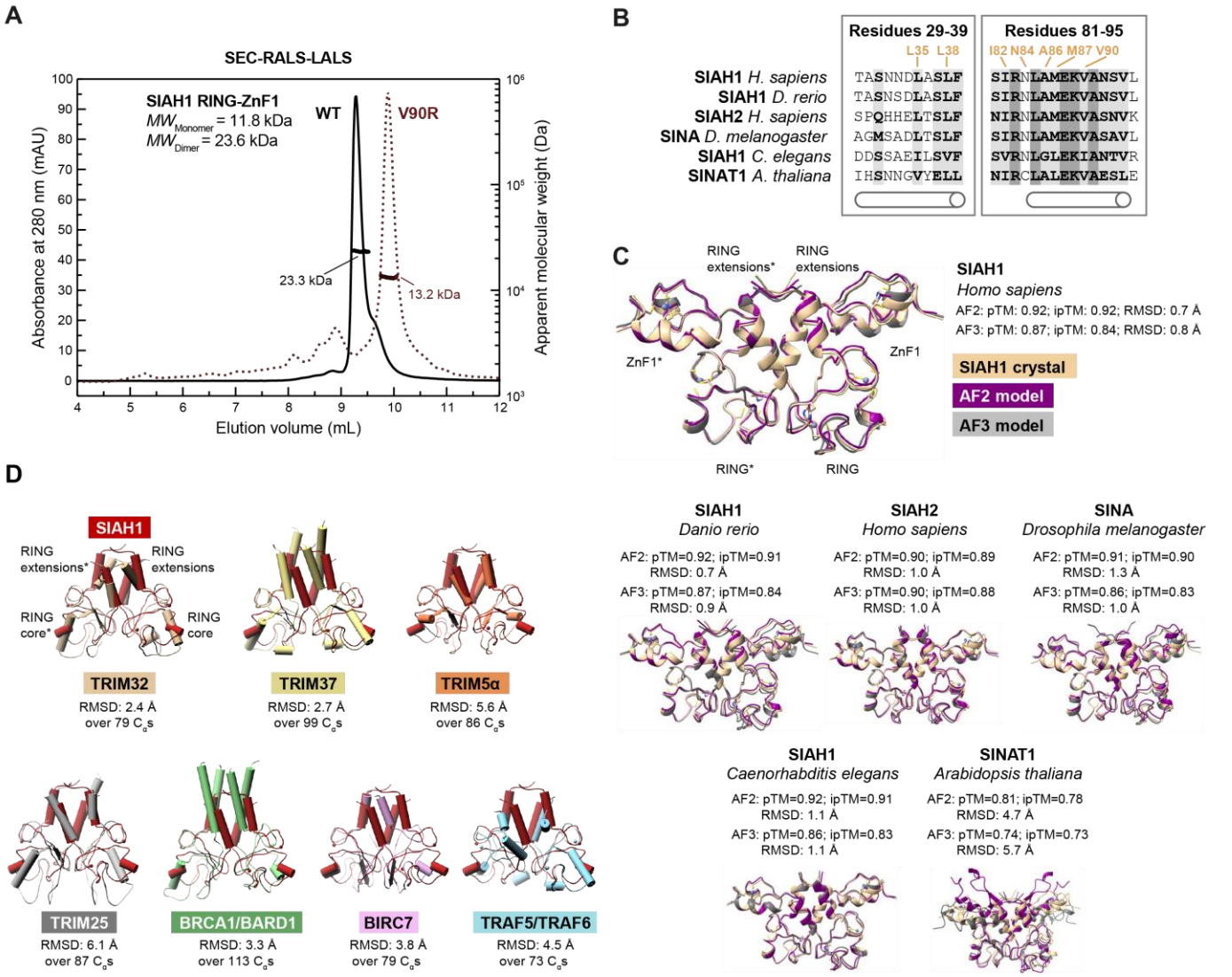

Figure 2 | RING dimerisation within SIAH1 and other SINA/SIAH subfamily members. (A) Size-exclusion chromatography coupled with right- and small-angle laser light scattering of the oligomerisation state of SIAH1 RING-ZnF1 injected at the starting concentration of 845 µM. A representative result of *n* = 2 particular experiments is shown. Superimposed SEC chromatograms of wild-type (WT; solid line, black) and mutant (V90R; dashed line, maroon) forms of the RING-ZnF1 fragment of SIAH1. The apparent molecular weight across the peaks calculated based on static light scattering is shown a thick line/series of dots (black for wild-type, maroon for V90R), and the calculated average apparent molecular weight is indicated. Theoretical molecular weights of monomer and dimer of SIAH1 RING-ZnF1 are provided ($MW_{Monomer}$ and MW_{Dimer}). **(B)** Two fragments of a multiple-sequence alignment of the indicated SINA/SIAH proteins, with invariant and conserved residues highlighted with dark and light grey boxes, respectively. Residues involved in the dimer interface are labelled in orange. The sequences considered for alignment were those of SIAH1_HUMAN (UniProt ID: Q8IUQ4), SIAH1_DANRE (UniProt ID: Q7ZVG6), SIAH2_HUMAN (UniProt ID: O43255), SINA_DROME (UniProt ID: P21461) SIAH1_CAEEL (UniProt ID: Q965X6) and SINA1_ARATH (UniProt ID: P93748). Sequences were aligned with Clustal Omega. A full-length multiple sequence alignment is provided in Supplementary Figure 1. **(C)** Ribbon diagrams showing structural superposition between the crystal dimer of the RING-ZnF1 fragment of human SIAH1 (light pink) and AlphaFold 2 (AF2, purple) and AlphaFold 3 (AF3, grey) models of dimeric forms of RING-ZnF1 fragments of indicated SINA/SIAH1 proteins. The best out of five models calculated with each programme is shown. For human SIAH1, all five models obtained with either AlphaFold version are additionally provided in Supplementary Figure 2. Confidence metrics pTM (predicted template modelling score) and ipTM (interface predicted template modelling score) for the shown models are provided. Root-mean-square-devation (RMSD) values corresponding to structural alignments (performed over all C_α atoms) between each model and the dimer derived from our SIAH1 crystal structure are provided. **(D)** Structural comparison of the RING dimers of SIAH1 and other dimeric RING-type E3 ligases in cylindrical representation. The RING dimer derived from our crystal structure of the RING-ZnF1 fragment of SIAH1 (coloured in dark red) is structurally aligned with RING dimers of various RING-type E3 ligases. Protein Data Bank entries used for this figure include 5FEY (TRIM32, beige), 3LRQ (TRIM37, yellow), 4TKP (TRIM5α, orange), 5EYA (TRIM25, grey), 1JM7 (BRCA1/BARD1, green), 4AUQ (BIRC7, pink), and 7L3L (TRAF5/6, light blue). See the main text for references. Root-mean-square-deviation (RMSD) values over the indicated number of C_α atoms (C_αs) are provided.

asymmetric units, which might reflect a solution homodimer mediated by the RING domain.

Experimental and bioinformatic analysis of RING dimerisation in SINA/SIAH E3 ligases

To determine if the crystallised SIAH1 fragment forms a dimer in solution, we injected the protein onto an analytical size-exclusion chromatography (SEC) column at a starting concentration of 845 µM, observing a single main elution peak (**Figure 2A**). We used a coupled right- and low-angle light scattering (RALS-LALS) instrument to measure the apparent molecular weight across the peak. The obtained value, 23.3 ± 0.3 kDa, is in excellent agreement with the expected molecular weight of a RING-ZnF1 dimer (23.6 kDa). We also analysed a version of the RING-ZnF1 fragment carrying a V90R mutation.

This mutation replaces the crystal dimerisation interface residue Val90 with a bulky and charged arginine that should sterically disable dimerisation. Equivalent mutations have been used to disrupt RING dimers made by tripartite motif (TRIM) RING E3 ligases (*e.g.*, I77R in TRIM5α [33] and V72R in TRIM25 [34]). The main peak for the V90R RING-ZnF1 fragment – injected at the same starting concentration as the WT protein – eluted later than that for the WT version, and the apparent molecular weight estimated with RALS-LALS was 13.2 ± 0.2 kDa, reasonably close to the expected value for a monomer (11.8 kDa). These observations suggest that the RING domain of SIAH1 forms homodimers that can be disrupted by the V90R mutation.

To estimate if the uncovered RING homodimerisation propensity might be conserved in other members of the SINA/SIAH subfamily of RING-type E3 ligases, we first performed a multiple sequence alignment of fragments of SINA/SIAH protein sequences corresponding to the extended RING domain (**Supplementary Figure 1**). We included sequences from a vascular plant (SINAT1 from *Arabidopsis thaliana*), a worm (SIAH1 from *Caenorhabditis elegans*), an insect (SINA from *Drosophila melanogaster*), a fish (SIAH1 from *Danio rerio*), and humans (SIAH1 and SIAH2). The sequence identity across the extended RING domains, *vis a vis* human SIAH1, ranges from 54% for SINAT1, through 68% for SIAH1 from *C. elegans* and 78% for both SINA from *D. melanogaster* and human SIAH2, to 99% for SIAH1 from *D. rerio*.

The fragments of the alignment corresponding to the α-helical RING extensions implicated in dimer formation are shown in **Figure 2B**. Notably, the four key hydrophobic residues mentioned above (Leu35, Leu38, Met87, and Val90) are either conserved or replaced by other hydrophobic amino acids in all analysed proteins, indicating that the propensity to dimerise is likely a shared feature of RING domains within this ligase subfamily. Moreover, the α-helical extension at the C-terminal side of RING (residues 81-94) is very highly conserved across its whole length, standing out as one of the most invariant regions in the entire ligase (**Supplementary Figure 1)**.

We moved on to performing structural modelling of dimeric forms of RING-ZnF1 regions using AlphaFold 2 Multimer 3 accessed *via* the ColabFold platform [35–37] or AlphaFold 3 accessed via the AlphaFold Server [38]. For each sequence, we generated five models. Of note, the protein data bank (PDB) structure database used as a training set did not contain our crystal structure, although it did contain several other RING domain dimers. We began with our crystallised human SIAH1 fragment, modelling a structure corresponding to two copies of its sequence (without the tag). AlphaFold 2 and AlphaFold 3 predicted a dimeric RING arrangement virtually identical to that in our crystal structure, even with respect to the relative angle between RING and ZnF1 domains, as reflected in the low root-mean-square-deviation (RMSD) between the models and the dimer derived from our crystal structure over all C_α atoms (see the top model in **Figure 2C** and all five, highly similar, models in **Supplementary Figure 2**). The dimeric models have very high interface predicted template modelling (ipTM) score values of 0.92 (for AlphaFold 2) or 0.84 (for AlphaFold 3), which indicates reliable predictions.

We extended this strategy to RING-ZnF1 fragment sequences of all SINA and SIAH proteins included above in the sequence alignment. For all of them, AlphaFold 2 generated dimeric models similar to our crystal structure (**Figure 2C**). The ipTM scores for the best models ranged from 0.78 to 0.92 (**Figure 2C**). RING dimerisation is very similar in all these models, but the angle between RING and ZnF1 varies across larger evolutionary distances, giving rise to higher RMSD values when comparing the models of more distant homologues, particularly SINAT1, to our crystal dimer. These differences might reflect model inaccuracy or genuine differences in the relative position of these two domains in different homologues. AlphaFold 3 produced similar results for RING-ZnF1 fragments of all six homologues, with slightly lower but still high ipTM scores for the best model ranging from 0.73 to 0.88.Finally, we compared the dimeric structure of the RING domain in SIAH1 to the hetero- and homodimers formed by RING domains in various other human RING-type E3 ligases, including the BRCA1:BARD1 [39] and TRAF5:TRAF6 [40] RING heterodimers, and the RING homodimers of TRIM32 [34], TRIM37 (PDB **3LRQ**, unpublished), TRIM5α [33], TRIM25 [34,41], and BIRC7 [42] (**Figure 2D**). The RING dimer in SIAH1 exhibits a significant overall similarity to all the other analysed dimers, with the closest apparent resemblance to the RING dimers of TRIM32 and TRIM37 proteins.

Altogether, the combined results of crystallography, solution light-scattering analysis, sequence alignment, and computational structural modelling point to RING-mediated homodimerisation being a feature of SIAH1 and likely a conserved property of the SINA/SIAH proteins across species, from plants to humans. The RING domains of these proteins appear to dimerise in a manner similar to that of other, previously characterised RING-type E3 ligases.

Modelling full-length SIAH1 and its higher-order organisation

We moved on to the modelling of the entire folded region of SIAH1 (RING-ZnF1-ZnF2-SBD, residues 28-282), disregarding the disordered N-terminal region encompassing residues 1-27. The construct that we studied above, RING-ZnF1, has the ZnF1 domain in common with the previously solved structures of the ZnF1-ZnF2-SBD fragment of SIAH1, allowing a confident structural alignment of the two fragments on ZnF1 (RMSD < 0.5 Å over ZnF1 C_α atoms) to produce a composite model of the entire folded part of SIAH1. The angle between ZnF2 and SBD is the same in three crystal structures of ZnF1-ZnF2-SBD solved in different space groups [28,29], suggesting a fixed relative orientation of these two domains. On the other hand, the angle between ZnF1 and ZnF2 varies in the three ZnF1-ZnF2-SBD crystal structures, indicating the presence of a flexible hinge that divides the structure of SIAH1 into two apparent rigid bodies: RING-ZnF1 and ZnF2-SBD. Therefore, depending on which of the previous ZnF1-ZnF2-SBD crystal structures is used, the composite model of RING-ZnF1-ZnF2-SBD differs in its overall conformation (**Figure 3A**). Of note, the composite model obtained by structural alignment of crystal structures is similar to AlphaFold 2 and AlphaFold 3 models of full-length SIAH1 (**Figure 3B**, **Supplementary Figure 3**).

We next considered the potential multimerisation of full-length SIAH1. In addition to RING-domain dimerisation uncovered

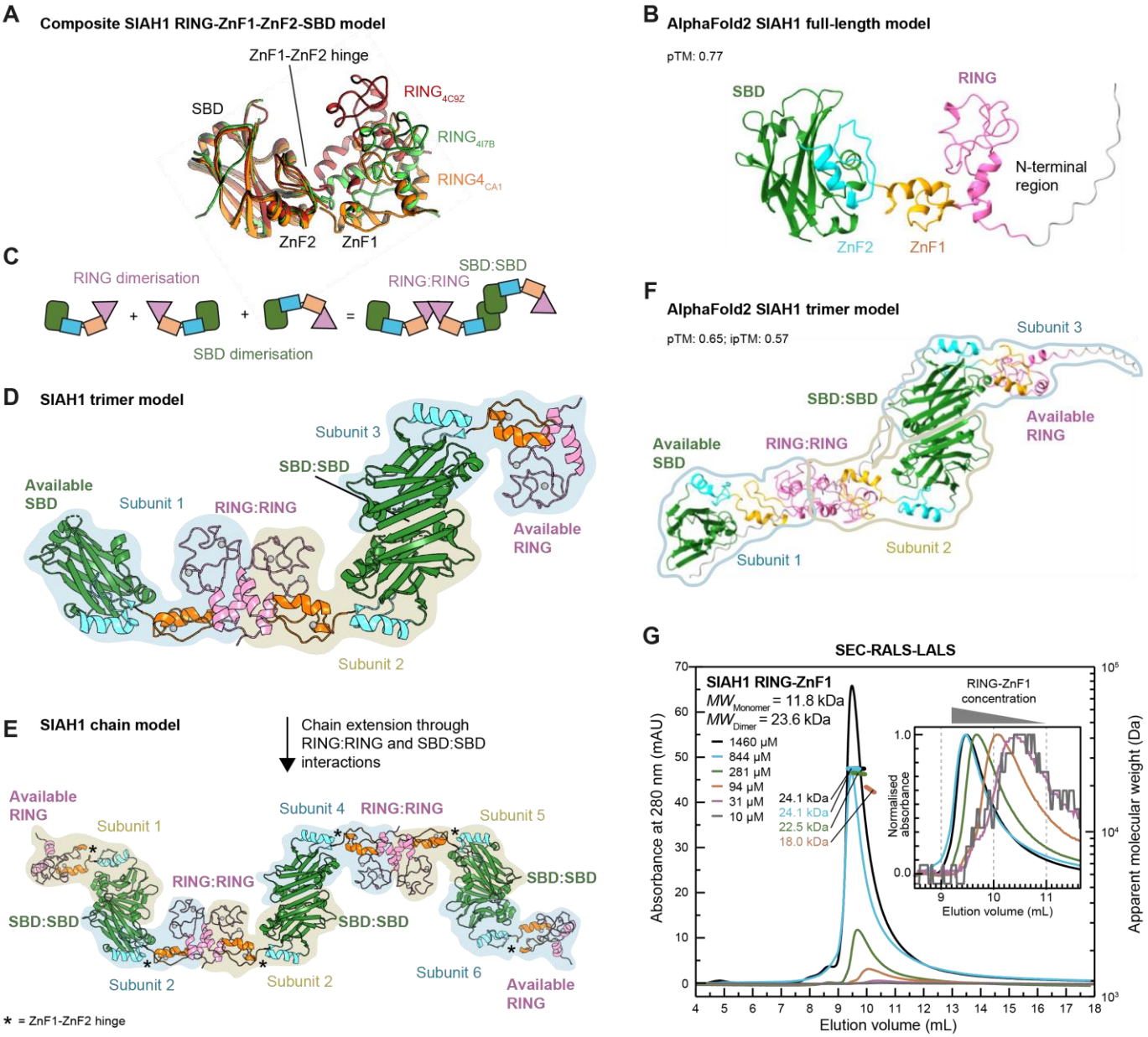

Figure 3 | Predicted open-ended multimerisation of full-length SIAH1. (A) A ribbon diagram of structural models of full-length human SIAH1 (except for residues 1-27) obtained by structural alignment of three different previously available ZnF1-ZnF2-SBD crystal structures (Protein Data Bank entries 4C9Z, 4I7B, 4CA1) on the SBD domain (root-mean-square-deviations < 0.75 Å over C_α atoms of the SBD domain) and subsequent alignment of each of them with our RING-ZnF1 structure on ZnF1 (root-mean-square-deviations < 0.5 Å over C_α atoms of the ZnF1 domain) in order to model in the RING domain. The final models are coloured red, green, or yellow, corresponding to the ZnF1-ZnF2-SBD structures 4C9Z, 4I7B, 4CA1, respectively. **(B)** A ribbon diagram of an AlphaFold 2 model of full-length human SIAH1 coloured according to domain composition like in Figure 1A. A top out of five generated models is shown here, whereas all five models are provided in Supplementary Figure 3. pTM (predicted template modelling score) is provided. **(C)** A schematic diagram showing the predicted multimerisation of full-length SIAH1 through simultaneous RING- and SBD-domain dimerisation. **(D)** A ribbon diagram of a trimer of human SIAH1 molecules (full-length except for residues 1-27). SIAH1 models were obtained like in A (using the crystal structure from this study and the Protein Data Bank entry 4CA1). The RING:RING and SBD:SBD contacts between SIAH1 molecules mirror dimerisation interfaces observed in our and 4CA1 crystal structures. Each SIAH1 subunit is coloured according to domain composition like in Figure 1A, with RING in pink, ZnF1 in orange, ZnF2 in blue, and the SBD domain in green. **(E)** A structural model of a longer SIAH1 multimer generated like in panel D. **(F)** Ribbon diagram of an AlphaFold 2 model of a trimer of full-length human SIAH1. Each SIAH1 subunit is coloured according to domain composition like in Figure 1A, with RING in pink, ZnF1 in orange, ZnF2 in blue, and the SBD domain in green. A top out of five generated models is shown here, while all five models are provided in Supplementary Figure 4. pTM (predicted template modelling) and ipTM (interface predicted template modelling) scores for the shown model are provided. **(G)** Size-exclusion chromatography coupled with right- and small-angle laser light scattering of the oligomerisation state of SIAH1 RING-ZnF1 injected at the indicated starting concentrations. A representative result of $n = 2$ particular experiments is shown. The apparent molecular weight across the main SEC peaks for selected concentrations are indicated as estimated based on the processed static light scattering signals (thick lines). Inset are fragments of normalised SEC profiles, where each peak's absorbance is scaled to the same height to facilitate elution volume comparison. Theoretical molecular weights (*MW*) of monomer and dimer of SIAH1 RING-ZnF1 are provided. Structural figures were created in PyMol (B, D, E) or Chimera (A, F).

here, SIAH1 has been reported to dimerise through its C-terminal SBD domain, which consistently forms an extensive two-fold rotationally symmetric homodimerisation interaction in all available ZnF1-ZnF2-SBD or ZnF2-SBD crystal structures, despite crystallising in various space groups [18,20,22,28–30]. The dimerisation of a ZnF1-ZnF2-SBD

fragment has been validated in solution using SEC and analytical ultracentrifugation [18].

The two SIAH1 dimerisation interfaces identified on RING and SBD domains are located at two extremities of the composite structure, facing away from each other. Therefore, even allowing for some flexibility at the ZnF1-ZnF2 hinge, it is sterically improbable for the RING and SBD domains of a SIAH1 molecule to be bound by RING and SBD domains of the same SIAH1 partner to form a closed SIAH1:SIAH1 dimer. Instead, each of these two interfaces is likely to bind to a different SIAH1 partner, resulting in a SIAH1:SIAH1:SIAH1 arrangement (**Figure 3C**). We constructed a model of this potential SIAH1 trimer through structural alignment of RING-ZnF1 and ZnF1-ZnF2-SBD dimers derived from crystal structures on the shared ZnF1 domain. The result produces an extended, open-ended trimer structure in which the terminal SBD and RING domains are available for binding to further SIAH1 molecules (**Figure 3D**), potentially producing long chains formed through alternating RING:RING and SBD:SBD interactions (see **Figure 3E** for a model, obtained in the same manner, of a chain comprising six SIAH1 subunits). Topologically, such filaments would be reminiscent of those formed by Speckle Type BTB/POZ Protein (SPOP) through its two dimerisation domains [43,44]. The flexibility at the ZnF1-ZnF2 hinge located at the centre of the SIAH1 protein would allow bending of such potential chains. Considering the high conservation of SINA/SIAH proteins, we expect that the proposed open-ended multimerisation is a feature of many and perhaps all family members, not just SIAH1.

As an alternative approach to assessing higher-order organisation of SIAH1, we employed AlphaFold 2 and AlphaFold 3 to predict a model of a SIAH1 trimer. In five out of five models, the structure prediction programme aligned three SIAH1 molecules into a chain (**Figure 3F, Supplementary Figure 4**), consistent with our hypothesis formulated based on structural alignments.

We have been unable to directly investigate the hypothesised higher-order assembly using recombinant protein, as, in our hands, SIAH1 fragments containing both RING and SBD portions showed poor expression and solubility in bacteria, which might be linked to its predicted open-ended multimerisation propensity.

Comparing RING- and SBD-mediated interactions

In the above-invoked example of the protein SPOP, which also homomultimerises through two distinct interfaces, the two interactions exhibit markedly different affinities, with SPOP chains effectively corresponding to medium-affinity associations between high-affinity dimeric building blocks [43]. We wondered whether the potential SIAH1 homomultimers share similar characteristics. Supporting this possibility, a previous analysis of SBD:SBD homodimerisation *via* analytical ultracentrifugation of a ZnF1-ZnF2-SBD fragment revealed high-affinity dimers, likely with a K_D in a nanomolar range [18].

To explore this further, we first performed a bioinformatic analysis of the RING and SBD homidimerisation interfaces using the PISA server [45] (**Table 2**). Previously, RING domains of the TRIM E3 ligase subfamily were shown to vary with respect to dimer stability in solution in a way that apparently correlates with the solvation energy gain upon dimerisation [15,46], a parameter that can be estimated using PISA and reflects burying of hydrophobic surfaces. Thus, strongly dimerising RING domains of TRIM69 and TRIM32 were predicted to have the most negative values of the solvation energy gain (–25 kcal/mol and –14.7 kcal/mol, respectively), while more transiently/weakly dimerising RINGs of TRIM23 or TRIM25 showed less negative values of approximately –10 kcal/mol. The PISA analysis of the SIAH1 RING dimerisation interface revealed that it is also largely hydrophobic, and its solvation energy gain upon dimerisation is around –13.7 kcal/mol. This value, falling between previously described extremes, suggests a moderate homodimerisation tendency of the SIAH1 RING domain. We also compared the SIAH1 RING homodimerisation interface parameters to those of the SBD, estimated based on the highest-resolution structures of the ZnF1-ZnF2-SBD dimer [18,28]. The SBD dimerisation interface is considerably larger, measuring around 1000 Å^2 or more depending on the structure, compared to approximately 800 Å^2 for the RING interface. Moreover, the SBD:SBD interaction – which involves the addition of two β-sheets – is very rich in hydrogen bonds and salt bridges but has a minimal solvation energy gain due to hydrophobic residues.

To experimentally evaluate the affinity of RING-mediated interactions, we performed SEC analysis of the SIAH1 RING-ZnF1 fragment at various starting concentrations ranging from 1460 µM to 10 µM (**Figure 3G**). Due to dilution during SEC, final protein concentrations on the column are expected to be considerably lower than the starting values. In this analysis, the RING-containing fragment exhibited a progressive shift in elution volume as the starting concentration decreased, becoming noticeable at injection concentrations of 281 µM and below. Moreover, static light scattering measurements revealed a decrease in the apparent molecular weight below the theoretical dimer weight for the lowest starting concentrations at which this estimation was possible, 281 µM and 94 µM. Together, these results suggest that the SIAH1 RING homodimer is unstable at low concentrations and might have a micromolar-range affinity, in contrast to the SBD:SBD dimer, which remained stable even at low micromolar concentrations in a previous analysis [18].

In summary, the combined evidence from prior studies on the SBD and our new data on the RING, supplemented by bioinformatic analysis, suggests that the proposed SIAH1 homomultimers can be viewed as high-affinity SBD-mediated dimers connected through weaker, more transient RING:RING interactions, with the former stabilised by polar contacts and the latter driven by the burial of hydrophobic residues.

RING dimerisation-dependent clustering of SIAH and SINA proteins in cells

Proteins endowed with a propensity to form open-ended chain-like homomultimers tend to cluster in distinct locations inside cells [43,47,48]. To investigate whether SIAH1 exhibits this behaviour and, if so, whether it depends on both RING and SBD dimerisation interfaces, we transiently overexpressed different N-terminally monomeric Cherry (mCherry)-tagged SIAH1 variants in U2OS cells, a human osteosarcoma cell line well-suited for cell imaging due to its flat morphology (**Figure 4A**). In this setup, the fluorescently-labelled full-length WT SIAH1 protein localised to distinct bright elongated cytoplasmic structures reminiscent of protein filaments, in contrast to a

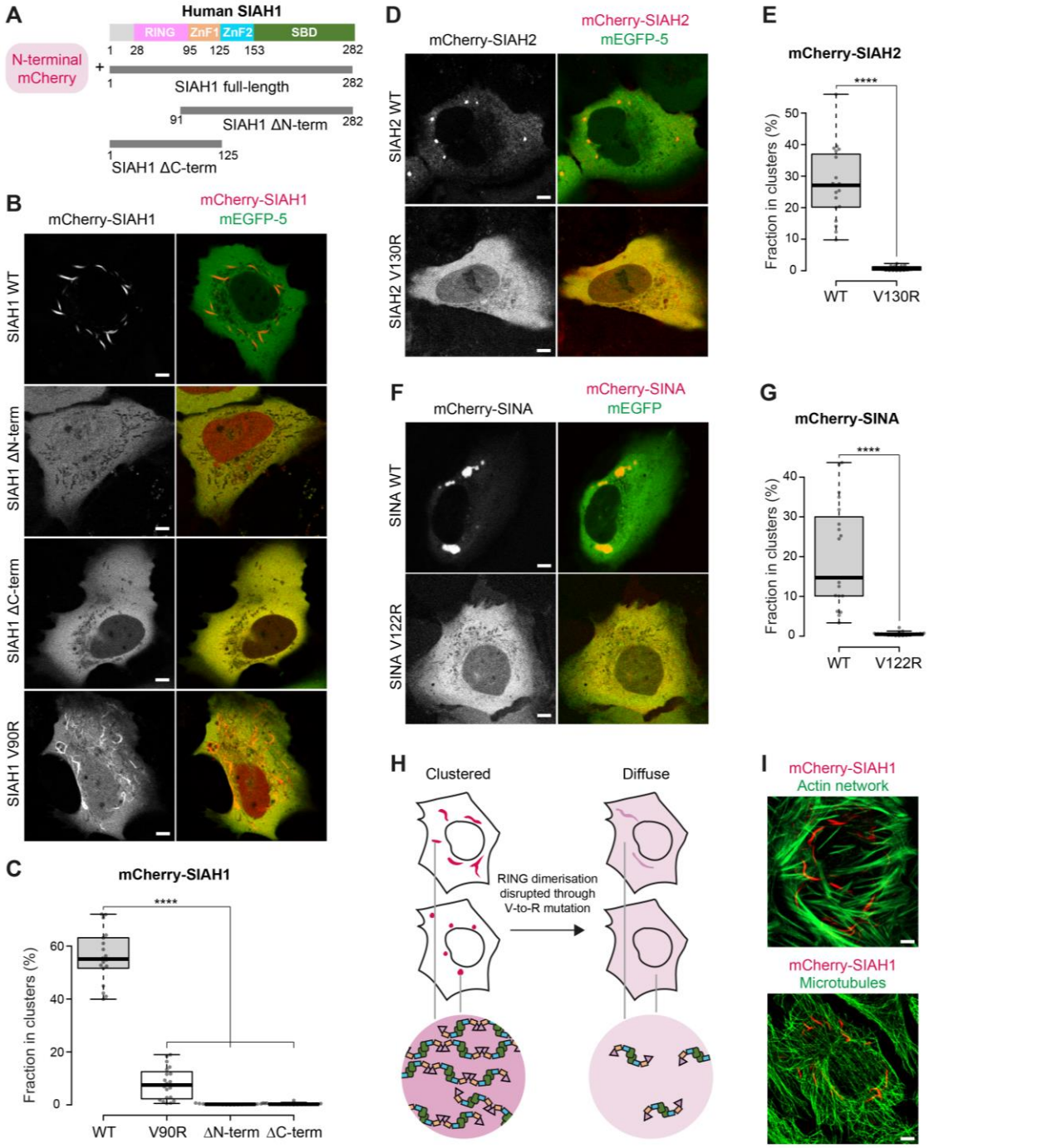

Figure 4 | Subcellular localisation analysis of SINA/SIAH proteins. (A) Domain architecture of the full-length human SIAH1 and the two truncated constructs, together with their names used in other panels. **(B)** Representative confocal images of live cells expressing wild-type (WT), V90R, or truncated (N-terminally or C-terminally) mCherry-SIAH1. In the merged image, colocalisation with an mEGFP-5 (composed of five fused EGFP proteins) control is shown. An additional set of representative cell images for this experiment is shown in Supplementary Figure 5. **(C)** Quantification of the fraction of mCherry-SIAH1 present in clusters (filaments) in the experiment presented in panel B, performed over $n = 18$ to 20 cells per condition. **(D)** Representative confocal images of live cells expressing wild-type (WT) or V130R mCherry-SIAH2. In the merged image, colocalisation with free mEGFP-5 is shown. Additional representative cell images for this experiment is shown in Supplementary Figure 5. **(E)** Quantification of the fraction of mCherry-SIAH2 present in clusters (foci/bodies) in the experiment presented in panel D, performed over $n = 19$ cells per condition. **(F)** Representative confocal images of live cells expressing wild-type (WT) or V122R mCherry-SINA. In the merged image, colocalisation with free mEGFP-5 is shown. Additional representative cell images for this experiment is shown in Supplementary Figure 5. **(G)** Quantification of the fraction of mCherry-SINA present in clusters (foci/bodies) in the experiment presented in panel F, performed over $n = 18$-19 cells per condition. **(H)** A tentative model in which the ability of SINA/SIAH proteins to form homomultimers *via* alternating RING:RING and SBD:SBD homotypic interactions contributes to the localisation of these proteins into distinct cellular locales. The postulated homomultimers are likely further noncovalently crosslinked by other factors (omitted for simplicity) resulting in bulky structures. In agreement with this model, the three analysed proteins become more diffusely distributed when the RING:RING interaction is disrupted through the V-to-R mutation. **(I)** Representative confocal images of fixed cells expressing wild-type (WT) mCherry-SIAH1 costained for the actin (top) or microtubule (bottom) networks. All scale bars in cell images correspond to 5 µm. All box plots show minimum (lower whisker), first quartile (lower box edge), median (thick line), third quartile (upper box edge), and maximum (upper whisker). **** represents p value < 0.0001 according to a two-sided Student's t test, assuming unequal variances. For all cell biology experiments, a representative result from $n = 3$ particular repeats of the experiment are shown.

arranged monomeric enhanced GFP molecules (mEGFP-5), which homogeneously stains the cell cytoplasm while being largely excluded from the nucleus (**Figure 4B** and **Supplementary Figure 5**). We next compared the WT protein with two truncations lacking either the RING or the SBD dimerisation domain. To ensure that the truncated forms are not misfolded, we used the same truncation sites as in the crystallised fragments, which are known to be stable; the only difference compared to the crystallised fragments was that the N-terminal disordered region was included in the C-terminally truncated form (SIAH1 ΔN term comprising residues 91-282 and SIAH1 ΔC term comprising residues 1-125; **Figure 4A**). When overexpressed as N-terminally mCherry-fused constructs, both of these truncated forms of SIAH1 showed diffuse distribution (**Figure 4B** and **Supplementary Figure 5**). The RING-ZnF1 fragment (SIAH1 ΔC term) was mos tly cytoplasmic, whereas the ZnF1-ZnF2-SBD fragment (SIAH1 ΔN term) was uniformly distributed across the entire cell. The shift to a diffuse distribution is consistent with the model where both dimerisation domains must be simultaneously present to allow the proposed open-ended clustering of SIAH1 molecules.

We also tested a full-length mCherry-tagged SIAH1 variant that carried the validated RING dimerisation-deficient V90R mutation. This mutation largely abrogated SIAH1 ability to accumulate into clusters, although some filaments could still be observed concomitantly to the predominant diffuse cytoplasmic staining (**Figure 4B** and **Supplementary Figure 5**). Quantifying the proportion of fluorescently-tagged SIAH1 accumulating in clusters confirmed the dramatic decrease in clustering propensity for the V90R mutant (**Figure 4C**). This change in SIAH1 localisation caused by the V90R mutation underscores the important role of RING-mediated interactions in cellular SIAH1 clustering.

Furthermore, we performed an analogous subcellular localisation analysis of human SIAH2 (**Figure 4D, E**) and fruit fly SINA (**Figure 4F, G**), by looking at their N-terminally mCherry-tagged full-length constructs, expressed in human U2OS cells. We compared the localisation of the WT forms of these proteins to their mutant forms carrying a V-to-R substitution in a position equivalent to Val90 of SIAH1 (V130R for SIAH2, V122R for SINA). Both SIAH2 WT and SINA WT localised to distinct cytoplasmic bodies. Upon the V-to-R mutation, both proteins shifted completely to a diffuse cellular distribution with a predominant accumulation in the cytoplasm, in line with the conservation of RING dimerisation and the proposed clustering model within the SINA/SIAH subfamily of RING-type E3 ligases (**Figure 4H**).

We also wondered whether the filament-like shape observed for the SIAH1 clusters could be triggered by SIAH1's interaction with the cytoskeleton. However, we did not observe specific colocalisation between the SIAH1 structures and the actin and microtubule networks (**Figure 4I**), leaving the origin of the elongated shape of the clusters formed by this particular member of the SINA/SIAH subfamily uncertain.

RING dimerisation-dependent colocalisation of SIAH1 with aggregated synphilin-1

SIAH1 has been reported to ubiquitylate and promote the degradation of synphilin-1, a protein found in Lewy bodies in Parkinson's patients [26,51,52]. Moreover, when the proteasome is inhibited, SIAH1 has been observed to colocalise with synphilin-1 and facilitate the formation of synphilin-1 inclusions [26,52].

We have revisited this topic using U2OS cells cotransfected with vectors expressing mCherry-tagged SIAH1 and eGFP-tagged aggregation-prone isoform of synphilin, synphilin-1A [52,53]. Upon proteasomal inhibition with MG132, we observed heterogeneous aggregates of synphilin-1A, as illustrated by images of two representative cells (**Figure 5A**). While these aggregates partially colocalised with WT SIAH1, as previously reported, the colocalisation was strongly reduced with the V90R mutant (**Figure 5B**).

Although the colocalisation of SIAH1 and synphilin-1A was previously shown to require an intact zinc coordination by the SIAH1 RING domain [52], our result demonstrates the specific importance of RING-mediated homodimerisation – rather than just the integrity of the RING domain as such – for this phenomenon. This is consistent with a role of SIAH1 self-association in directing this E3 ligase to at least one established aggregation-prone substrate. Since the postulated RING- and SBD-mediated SIAH1 homomultimeric assemblies would contain multiple SBD domains in close proximity, they are expected to preferentially target multivalent (aggregated, polymeric, or oligomeric) substrates (**Figure 5C**).

Importance of RING dimerisation for SIAH1 ubiquitylation activity

To investigate whether RING dimerisation contributes not only to cellular clustering and substrate recruitment, but also to the catalytic activity of SIAH1, we performed an *in-vitro* ubiquitylation assay of the purified recombinant RING-ZnF1 fragment of SIAH1 characterised above. We incubated the WT or V90R variants with the main human E1 enzyme Ubiquitin-Activating Enzyme 1 (UBA1) and the E2 enzyme Ubiquitin-Conjugating Enzyme E2 D1 (UBE2D1/UbcH5a). The choice of this E2 enzyme was motivated by the fact that SIAH1 has been shown to work most efficiently with the UBE2D/UbcH5-family enzymes among several tested human E2s [27]. Since the SIAH1 fragment used in this experiment lacks the SBD responsible for substrate recruitment, no substrate was included; instead, we assessed catalytic activity by monitoring the production of free ubiquitin chains and the ubiquitylation of the E1, E2, and E3 proteins present in the mixture, as revealed using anti-ubiqutin immunoblotting (**Figure 6A**).

The activities of WT and V90R SIAH1 RING-ZnF1 were compared to a positive control (a reaction containing a catalytic fragment of the RING-type E3 ligase DTX3L [49,50]) and a negative control (a reaction performed without any E3 ligase). The results reveal marked differences in activity between the WT and V90R SIAH1 fragments. Specifically, the WT generates substantially more polyubiquitin chains in the course of the experiment. In contrast, the V90R variant shows an accumulation of shorter ubiquitin chains, likely because it fails to efficiently extend them to polyubiquitin chains.

To assess the contribution of dimerisation to the activity of full-length SIAH1 in cells, we monitored the colocalisation of transiently expressed mCherry-tagged full-length SIAH1 with K48-linked ubiquitin chains using mCherry fluorescence and ubiquitin immunostaining in fixed U2OS cells. Overexpression of SIAH1 WT was associated with a strong enrichment of

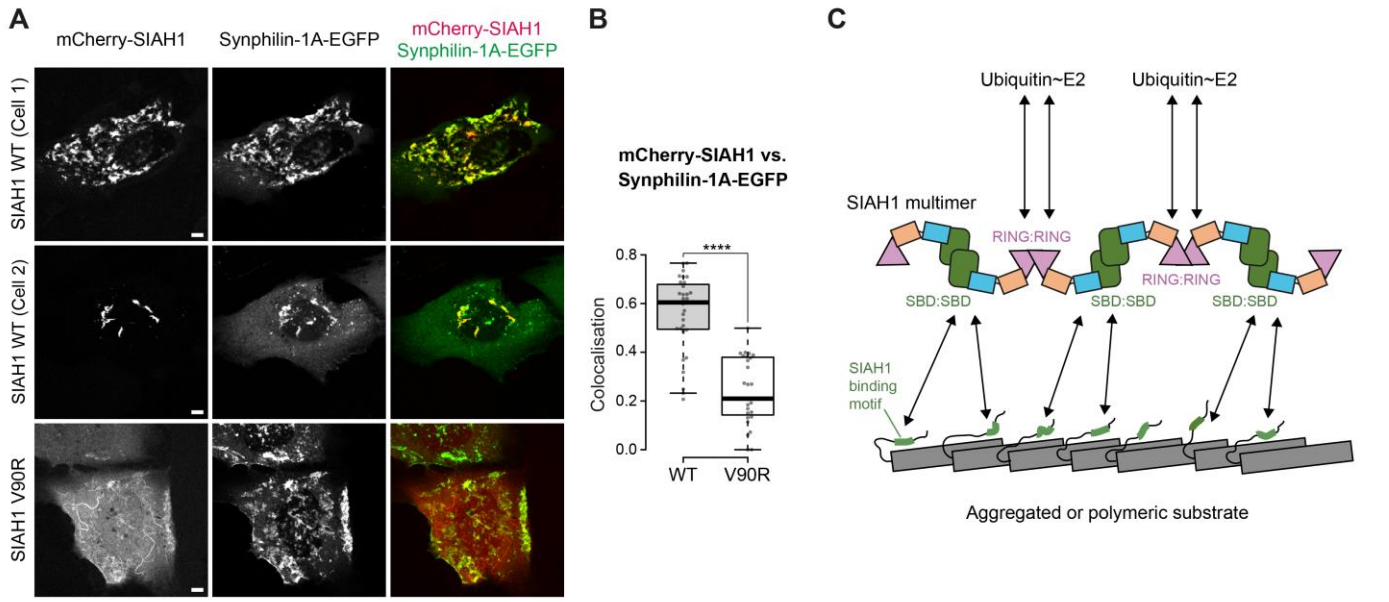

Figure 5 | The contribution of SIAH1 RING dimerisation to substrate recruitment. (A) Colocalisation of SIAH1 with aggregated synphilin-1A. Representative confocal images of live cells coexpressing wild-type (WT) or V90R mCherry-tagged SIAH1 and eGFP-tagged synphilin-1A and treated with 20 μM MG132 for 8 hours. For WT SIAH1, two different cells are shown. **(B)** Quantification of colocalisation (Pearson's correlation coefficient) of mCherry-SIAH1 with synphilin-1A in the experiment presented in panel A, performed over n = 28-32 cells per condition. The box plot shows minimum (lower whisker), first quartile (lower box edge), median (thick line), third quartile (upper box edge), and maximum (upper whisker). **** represents p value < 0.0001 according to a two-sided Student's t test, assuming unequal variances. **(C)** A tentative model of the role of SIAH1 multimerisation in the recruitment to multivalent protein substrates. SIAH1 molecules are coloured according to domain composition like in Figure 1A. SIAH1 is expected to self-organise into chain-like structures through alternating RING:RING and SBD:SBD contacts. This higher-order SIAH1 assembly could form multivalent interactions with a multimeric or aggregated protein substrate, each SBD domain engaging a SIAH-binding motif on a different substrate protomer. All scale bars in cell images correspond to 5 μm. For all cell biology experiments, a representative result from n = 3 particular repeats of the experiment are shown.

ubiquitin chains at SIAH1 clusters, likely reflecting ubiquitylation of SIAH1 itself as well as SIAH1-associated substrate proteins (**Figure 6B, C**). In contrast, no such polyubiquitin signal was observed at residual SIAH1 V90R filaments. These results suggest that, in the context of full-length SIAH1 in cells, RING dimerisation makes a major contribution to this enzyme's ubiquitylation output.

Lastly, we tested whether catalytic activity contributes to the subcellular localisation of mCherry-SIAH1 by comparing the WT protein with its catalytic mutant, R76A. This mutant contains an alanine substitution of the linchpin residue, which in other RING-type E3 ligases has been shown to play a key role in the stabilisation of the closed conformation of ubiquitin~E2 by simultaneously binding to both E2 and ubiquitin parts of this thioester intermediate [11]. The R76A mutation is located away from the RING dimerisation interface and is not expected to directly affect RING dimerisation. While the R76A mutant, like the WT SIAH1 protein, was still predominantly localised to filament-like structures, these filaments now appeared to be thinner and to clasp together in some parts of the cell, notably near the nuclear envelope (**Figure 6D, E**). The observed difference suggests that diminished SIAH1 ubiquitylation activity and/or diminished binding to ubiquitin~E2 only moderately impact the clustering propensity but affect the spatial organisation of these clusters.

Discussion

By solving the structure of the RING domain of SIAH1, we completed the experimental structural characterisation of individual elements of SINA/SIAH proteins. Aligning our structure with those of C-terminal SIAH1 fragments produces a composite full-length structure composed of two rigid bodies (RING-ZnF1 and ZnF2-SBD) separated by a hinge located between ZnF1 and ZnF2. The apparent flexibility of the RING-ZnF1 and ZnF2-SBD regions with respect to each other might provide necessary adaptability to correctly position protein substrates (recruited through SBD) *vis a vis* a loaded E2 enzyme (recruited through RING).

According to our crystal structure and solution light scattering-based analysis, the RING domain of SIAH1 forms homodimers similar to those in TRIM proteins and some other dimerising RING-type E3 ligases. The E2-interacting interfaces on the two SIAH1 RING domains in a dimer remain available for E2 binding. Our observations that RING dimerisation contributes to SIAH1's catalytic activity could suggest that the two RINGs cooperate, or, at the very least, mutually stabilise each other, to facilitate efficient synthesis of polyubiquitin chains. Importantly, our bioinformatic analysis suggests that RING dimerisation is a conserved feature of the SINA/SIAH subfamily of RING-type E3 ligases among various species.

Until now, SIAH1 has been described as a dimeric protein that self-associates through its C-terminal SBD domain [18]. The identification of RING-mediated dimerisation complicates this picture. Although the two interfaces have very different physico-chemical properties, homodimers formed through each of them appear relatively strong in solution. This makes it likely that full-length SIAH1 employs both interfaces simultaneously to assemble into oligo- or polymeric chains or rings, which could be seen as composed of stable SBD-mediated dimeric building blocks further oligomerising through weaker/more

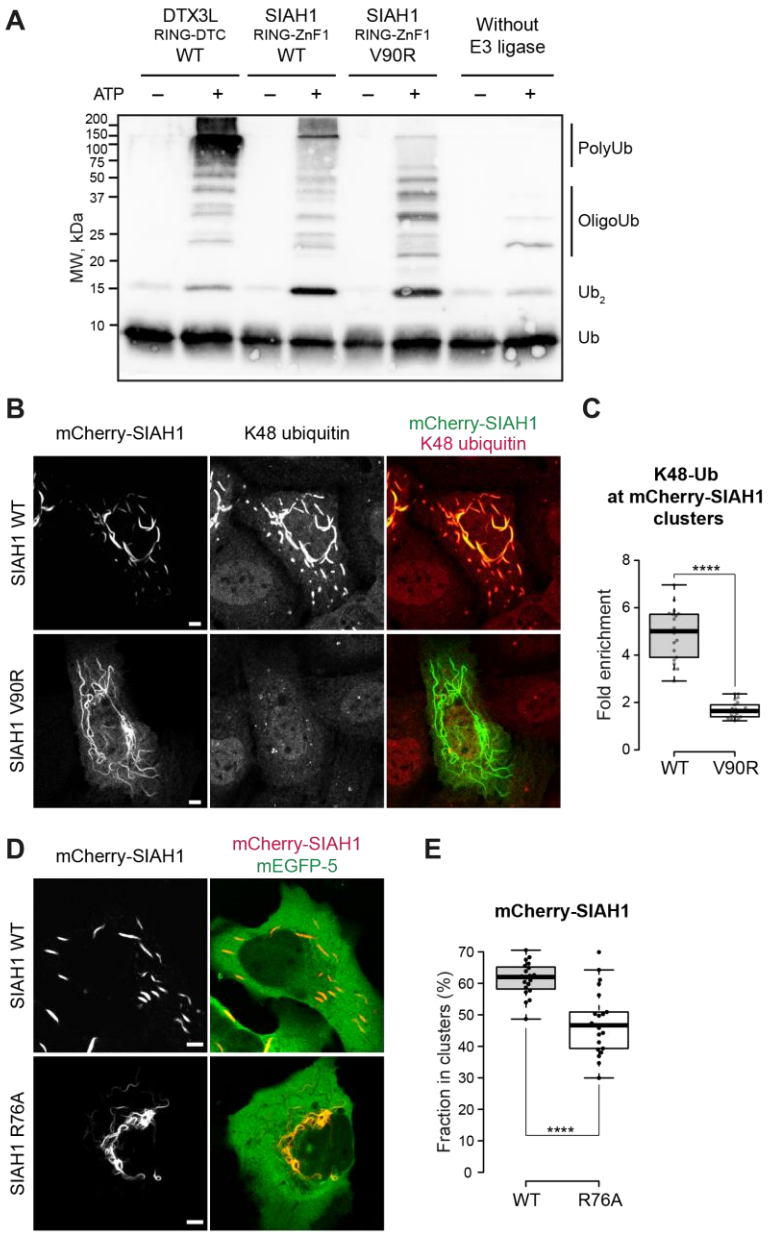

Figure 6 | The contribution of SIAH1 RING dimerisation to E3 ubiquitin ligase activity. (A) An *in-vitro* ubiquitylation assay performed by incubating ubiquitin, human E1 UBA1, E2 UBE2D1, the indicated E3 ligase fragment or no E3 ligase, in the presence or absence of ATP. The results were visualised using an anti-ubiquitin primary antibody P4D1. Ub, ubiquitin. A representative result of $n = 3$ experiments is shown. **(B)** Colocalisation of SIAH1 with K48-linked ubiquitin. Representative confocal images of fixed cells expressing wild-type (WT) or V90R mCherry-tagged SIAH1 costained with an anti-K48-linked ubiquitin antibody. **(C)** Quantification of the enrichment of K48-linked ubiquitin on SIAH1 clusters (filaments) in the experiment presented in panel E, performed over $n = 22$ cells per condition. **(D)** Representative confocal images of live cells expressing wild-type (WT) or R76A (arginine linchpin mutant) mCherry-tagged SIAH1. In the merged image, colocalisation with free mEGFP-5 is shown. **(E)** Quantification of the fraction of mCherry-SIAH1 present in clusters (filaments) in the experiment presented in panel G, performed over $n = 20$-22 cells per condition. All scale bars in cell images correspond to 5 µm. All box plots show minimum (lower whisker), first quartile (lower box edge), median (thick line), third quartile (upper box edge), and maximum (upper whisker). **** represents p value < 0.0001 according to a two-sided Student's t test, assuming unequal variance. For all cell biology experiments, a representative result from $n = 3$ particular repeats of the experiment are shown.

transient RING:RING interactions. A similar behaviour – relying on RING dimerisation and an additional dimerisation or oligomerisation motif (typically a coiled coil) – has been proposed for some RING-type E3 ligases from the TRIM family when they coat a virus or a membrane [15,33,54,55]. Beyond E3 ligases, formation of higher-order filamentous oligomers through two dimerisation interfaces present in the same protein has been reported for the ubiquitin ligase adaptor protein SPOP [43,44] and zinc finger and Broad-Complex, Tramtrack, and Bric-à-brac (BTB) domain-containing (ZBTB) transcription factors [56].

From a practical point of view, the potential higher-order SIAH1 assemblies might partly explain the difficulties with obtaining soluble SIAH1 comprising both RING and SBD domains. As mentioned above, we have been unable to achieve this, and the relative scarcity of *in vitro* studies and no structural or biophysical studies involving purified full-length SIAH1 in existing literature suggests that it might be a more general problem. It is known that open-ended protein assemblies can become insoluble upon recombinant overexpression [47,57]. Finding a solution to this problem – one that allows obtaining sufficient amounts of high-quality samples – may hold the key to the future structural, biophysical, and functional characterisation of full-length SIAH1.

In the context of SIAH1 biology, the higher-order assembly facilitated by alternating RING- and SBD-mediated interactions likely underpins the clustering of SIAH1 and its homologues into distinct cytoplasmic structures in our live-cell experiments. The nonhomogeneous distribution of endogenous SIAH1 observed in immunostained fixed cell lines from the Human Protein Atlas [58] suggests that similar clusters form at endogenous protein levels, although they are likely to be less prominent compared to those seen in our overexpression setup. The clustering propensity seems to be a general feature of SINA/SIAH proteins, despite differences in the exact structures that they localise to. In particular, SIAH1 localises to elongated, filamentous structures (**Figure 4B**), which might depend on binding to another cellular factor, although this pattern seems unrelated to either actin or microtubule network (**Figure 4I**).

The multivalency afforded by such higher-order organisation could explain an apparent preference of SIAH1 for multimeric protein substrates [4]. In our model, some substrates – presumably those with a weak, low affinity SIAH1-binding degron – would only be efficiently ubiquitylated if they are present in an aggregated or polymeric form, because this allows simultaneous or cooperative binding of multiple weak degron copies to multiple SBD domains within a SIAH1 chain (**Figure 5C**). Multivalent recognition might explain the reported preferential ubiquitylation of the polymerised form of the oncoprotein BCL6 (induced by the small molecule BI-3802) by SIAH1 over the native, non-polymerised BCL6, which is known to contain a weak degron [27]. This mechanism could also account for SIAH1's targeting of aggregated forms of some proteins, such as synphilin-1A [26,52] (**Figure 5A-B**). A similar multivalency-based paradigm has been suggested for the recruitment of substrates to the ubiquitin ligase adaptor SPOP [59] and to a protein ADP-ribosylating enzyme, tankyrase

[60–63], both of which form open-ended filamentous structures *in vitro* and localise to distinct foci in cells. Interestingly, the signalling scaffold protein Axin – itself capable of open-ended multimerisation – is a substrate of both tankyrase [64] and SIAH1/SIAH2 [30], and it is possible that in both cases Axin may be recognised through multivalent interactions. This fascinating model, suggested by our structural and cellular analysis, should be further experimentally investigated in the future.

References

1 Suskiewicz MJ (2024) The logic of protein post-translational modifications (PTMs): Chemistry, mechanisms and evolution of protein regulation through covalent attachments. *BioEssays* **46**, 2300178.

2 Zheng N & Shabek N (2017) Ubiquitin Ligases: Structure, Function, and Regulation. *Annu Rev Biochem* **86**, 129–157.

3 Kozicka Z & Thomä NH (2021) Haven't got a glue: Protein surface variation for the design of molecular glue degraders. *Cell Chem Biol* **28**, 1032–1047.

4 Jevtić P, Haakonsen DL & Rapé M (2021) An E3 ligase guide to the galaxy of small-molecule-induced protein degradation. *Cell Chem Biol* **28**, 1000–1013.

5 Wu T, Yoon H, Xiong Y, Dixon-Clarke SE, Nowak RP & Fischer ES (2020) Targeted protein degradation as a powerful research tool in basic biology and drug target discovery. *Nat Struct Mol Biol* **27**, 605–614.

6 Luh LM, Scheib U, Juenemann K, Wortmann L, Brands M & Cromm PM (2020) Prey for the Proteasome: Targeted Protein Degradation—A Medicinal Chemist's Perspective. *Angew Chem Int Ed* **59**, 15448–15466.

7 Samarasinghe KTG & Crews CM (2021) Targeted protein degradation: A promise for undruggable proteins. *Cell Chem Biol* **28**, 934–951.

8 Metzger MB, Pruneda JN, Klevit RE & Weissman AM (2014) RING-type E3 ligases: Master manipulators of E2 ubiquitin-conjugating enzymes and ubiquitination. *Biochim Biophys Acta BBA - Mol Cell Res* **1843**, 47–60.

9 Reverter D & Lima CD (2005) Insights into E3 ligase activity revealed by a SUMO–RanGAP1–Ubc9–Nup358 complex. *Nature* **435**, 687–692.

10 Plechanovová A, Jaffray EG, Tatham MH, Naismith JH & Hay RT (2012) Structure of a RING E3 ligase and ubiquitin-loaded E2 primed for catalysis. *Nature* **489**, 115–120.

11 Pruneda JN, Littlefield PJ, Soss SE, Nordquist KA, Chazin WJ, Brzovic PS & Klevit RE (2012) Structure of an E3:E2~Ub Complex Reveals an Allosteric Mechanism Shared among RING/U-box Ligases. *Mol Cell* **47**, 933–942.

12 Branigan E, Carlos Penedo J & Hay RT (2020) Ubiquitin transfer by a RING E3 ligase occurs from a closed E2~ubiquitin conformation. *Nat Commun* **11**, 2846.

13 Goffinont S, Coste F, Prieu-Serandon P, Mance L, Gaudon V, Garnier N, Castaing B & Suskiewicz MJ (2023) Structural insights into the regulation of the human E2~SUMO conjugate through analysis of its stable mimetic. *J Biol Chem* **299**.

14 Budhidarmo R, Nakatani Y & Day CL (2012) RINGs hold the key to ubiquitin transfer. *Trends Biochem Sci* **37**, 58–65.

15 Fiorentini F, Esposito D & Rittinger K (2020) Does it take two to tango? RING domain self-association and activity in TRIM E3 ubiquitin ligases. *Biochem Soc Trans* **48**, 2615–2624.

16 Carthew RW & Rubin GM (1990) seven in absentia, a gene required for specification of R7 cell fate in the Drosophila eye. *Cell* **63**, 561–577.

17 Hu G, Chung YL, Glover T, Valentine V, Look AT & Fearon ER (1997) Characterization of human homologs of the Drosophila seven in absentia (sina) gene. *Genomics* **46**, 103–111.

18 Polekhina G, House CM, Traficante N, Mackay JP, Relaix F, Sassoon DA, Parker MW & Bowtell DDL (2002) Siah ubiquitin ligase is structurally related to TRAF and modulates TNF-α signaling. *Nat Struct Biol* **9**, 68–75.

19 House CM, Frew IJ, Huang H-L, Wiche G, Traficante N, Nice E, Catimel B & Bowtell DDL (2003) A binding motif for Siah ubiquitin ligase. *Proc Natl Acad Sci U S A* **100**, 3101–3106.

20 Matsuzawa S, Li C, Ni C-Z, Takayama S, Reed JC & Ely KR (2003) Structural Analysis of Siah1 and Its Interactions with Siah-interacting Protein (SIP) *. *J Biol Chem* **278**, 1837–1840.

21 House CM, Hancock NC, Möller A, Cromer BA, Fedorov V, Bowtell DDL, Parker MW & Polekhina G (2006) Elucidation of the substrate binding site of Siah ubiquitin ligase. *Struct Lond Engl 1993* **14**, 695–701.

22 Santelli E, Leone M, Li C, Fukushima T, Preece NE, Olson AJ, Ely KR, Reed JC, Pellecchia M, Liddington RC & Matsuzawa S (2005) Structural analysis of Siah1-Siah-interacting protein interactions and insights into the assembly of an E3 ligase multiprotein complex. *J Biol Chem* **280**, 34278–34287.

23 Dickins RA, Frew IJ, House CM, O'Bryan MK, Holloway AJ, Haviv I, Traficante N, de Kretser DM & Bowtell DDL (2002) The ubiquitin ligase component Siah1a is required for completion of meiosis I in male mice. *Mol Cell Biol* **22**, 2294–2303.

24 Frew IJ, Hammond VE, Dickins RA, Quinn JMW, Walkley CR, Sims NA, Schnall R, Della NG, Holloway AJ, Digby MR, Janes PW, Tarlinton DM, Purton LE, Gillespie MT & Bowtell DDL (2003) Generation and analysis of Siah2 mutant mice. *Mol Cell Biol* **23**, 9150–9161.

25 House CM, Möller A & Bowtell DDL (2009) Siah Proteins: Novel Drug Targets in the Ras and Hypoxia Pathways. *Cancer Res* **69**, 8835–8838.

26 Liani E, Eyal A, Avraham E, Shemer R, Szargel R, Berg D, Bornemann A, Riess O, Ross CA, Rott R & Engelender S (2004) Ubiquitylation of synphilin-1 and alpha-synuclein by SIAH and its presence in cellular inclusions and Lewy bodies imply a role in Parkinson's disease. *Proc Natl Acad Sci U S A* **101**, 5500–5505.

27 Słabicki M, Yoon H, Koeppel J, Nitsch L, Roy Burman SS, Di Genua C, Donovan KA, Sperling AS, Hunkeler M, Tsai JM, Sharma R, Guirguis A, Zou C, Chudasama P, Gasser JA, Miller PG, Scholl C, Fröhling S, Nowak RP, Fischer ES & Ebert BL (2020) Small-molecule-induced polymerization triggers degradation of BCL6. *Nature* **588**, 164–168.

28 Rimsa V, Eadsforth TC & Hunter WN (2013) Two high-resolution structures of the human E3 ubiquitin ligase Siah1. *Acta Crystallograph Sect F Struct Biol Cryst Commun* **69**, 1339–1343.

29 Stebbins JL, Santelli E, Feng Y, De SK, Purves A, Motamedchaboki K, Wu B, Ronai ZA, Liddington RC & Pellecchia M (2013) Structure-based design of covalent Siah inhibitors. *Chem Biol* **20**, 973–982.

30 Ji L, Jiang B, Jiang X, Charlat O, Chen A, Mickanin C, Bauer A, Xu W, Yan X & Cong F (2017) The SIAH E3 ubiquitin ligases promote Wnt/β-catenin signaling through mediating Wnt-induced Axin degradation. *Genes Dev* **31**, 904–915.

31 Middleton AJ, Budhidarmo R, Das A, Zhu J, Foglizzo M, Mace PD & Day CL (2017) The activity of TRAF RING homo- and heterodimers is regulated by zinc finger 1. *Nat Commun* **8**, 1788.

32 Bijlmakers M-J, Teixeira JMC, Boer R, Mayzel M, Puig-Sàrries P, Karlsson G, Coll M, Pons M & Crosas B (2016) A C2HC zinc finger is essential for the RING-E2 interaction of the ubiquitin ligase RNF125. *Sci Rep* **6**, 29232.

33 Yudina Z, Roa A, Johnson R, Biris N, de Souza Aranha Vieira DA, Tsiperson V, Reszka N, Taylor AB, Hart PJ, Demeler B, Diaz-Griffero F & Ivanov DN (2015) RING Dimerization Links Higher-Order Assembly of TRIM5α to Synthesis of K63-Linked Polyubiquitin. *Cell Rep* **12**, 788–797.

34 Koliopoulos MG, Esposito D, Christodoulou E, Taylor IA & Rittinger K (2016) Functional role of TRIM E3 ligase oligomerization and regulation of catalytic activity. *EMBO J* **35**, 1204–1218.

35 Mirdita M, Schütze K, Moriwaki Y, Heo L, Ovchinnikov S & Steinegger M (2022) ColabFold: making protein folding accessible to all. *Nat Methods* **19**, 679–682.

36 Jumper J, Evans R, Pritzel A, Green T, Figurnov M, Ronneberger O, Tunyasuvunakool K, Bates R, Žídek A, Potapenko A, Bridgland A, Meyer C, Kohl SAA, Ballard AJ, Cowie A, Romera-Paredes B, Nikolov S, Jain R, Adler J, Back T, Petersen S, Reiman D, Clancy E, Zielinski M, Steinegger M, Pacholska M, Berghammer T, Bodenstein S, Silver D, Vinyals O, Senior AW, Kavukcuoglu K, Kohli P & Hassabis D (2021) Highly accurate protein structure prediction with AlphaFold. *Nature* **596**, 583–589.

37 Evans R, O'Neill M, Pritzel A, Antropova N, Senior A, Green T, Žídek A, Bates R, Blackwell S & Yim J (2022) Protein complex prediction with AlphaFold-Multimer. *BioRxiv*, 2021–10.

38 Abramson J, Adler J, Dunger J, Evans R, Green T, Pritzel A, Ronneberger O, Willmore L, Ballard AJ, Bambrick J, Bodenstein SW, Evans DA, Hung C-C, O'Neill M, Reiman D, Tunyasuvunakool K, Wu Z, Žemgulytė A, Arvaniti E, Beattie C, Bertolli O, Bridgland A, Cherepanov A, Congreve M, Cowen-Rivers AI, Cowie A, Figurnov M, Fuchs FB, Gladman H, Jain R, Khan YA, Low CMR, Perlin K, Potapenko A, Savy P, Singh S, Stecula A, Thillaisundaram A, Tong C, Yakneen S, Zhong ED, Zielinski M, Žídek A, Bapst V, Kohli P, Jaderberg M, Hassabis D & Jumper JM (2024) Accurate structure prediction of biomolecular interactions with AlphaFold 3. *Nature* **630**, 493–500.

39 Brzovic PS, Rajagopal P, Hoyt DW, King MC & Klevit RE (2001) Structure of a BRCA1-BARD1 heterodimeric RING-RING complex. *Nat Struct Biol* **8**, 833–837.

40 Das A, Middleton AJ, Padala P, Ledgerwood EC, Mace PD & Day CL (2021) The Structure and Ubiquitin Binding Properties of TRAF RING Heterodimers. *J Mol Biol* **433**, 166844.

41 Sanchez JG, Chiang JJ, Sparrer KMJ, Alam SL, Chi M, Roganowicz MD, Sankaran B, Gack MU & Pornillos O (2016) Mechanism of TRIM25 Catalytic Activation in the Antiviral RIG-I Pathway. *Cell Rep* **16**, 1315–1325.

42 Dou H, Buetow L, Sibbet GJ, Cameron K & Huang DT (2012) BIRC7–E2 ubiquitin conjugate structure reveals the mechanism of ubiquitin transfer by a RING dimer. *Nat Struct Mol Biol* **19**, 876–883.

43 Marzahn MR, Marada S, Lee J, Nourse A, Kenrick S, Zhao H, Ben-Nissan G, Kolaitis R, Peters JL, Pounds S, Errington WJ, Privé GG, Taylor JP, Sharon M, Schuck P, Ogden SK & Mittag T (2016) Higher-order oligomerization promotes localization of SPOP to liquid nuclear speckles. *EMBO J* **35**, 1254–1275.

44 Cuneo MJ, O'Flynn BG, Lo Y-H, Sabri N & Mittag T (2023) Higher-order SPOP assembly reveals a basis for cancer mutant dysregulation. *Mol Cell* **83**, 731-745.e4.

45 Krissinel E & Henrick K (2007) Inference of Macromolecular Assemblies from Crystalline State. *J Mol Biol* **372**, 774–797.

46 Keown JR, Yang J, Black MM & Goldstone DC (2020) The RING domain of TRIM69 promotes higher-order assembly. *Acta Crystallogr Sect D* **76**, 954–961.

47 Bienz M (2020) Head-to-Tail Polymerization in the Assembly of Biomolecular Condensates. *Cell* **182**, 799–811.

48 Garcia-Seisdedos H, Empereur-Mot C, Elad N & Levy ED (2017) Proteins evolve on the edge of supramolecular self-assembly. *Nature* **548**, 244–247.

49 Chatrin C, Gabrielsen M, Buetow L, Nakasone MA, Ahmed SF, Sumpton D, Sibbet GJ, Smith BO & Huang DT (2020) Structural insights into ADP-ribosylation of ubiquitin by Deltex family E3 ubiquitin ligases. *Sci Adv* **6**, eabc0418.

50 Zhu K, Suskiewicz MJ, Chatrin C, Strømland Ø, Dorsey BW, Aucagne V, Ahel D & Ahel I (2024) DELTEX E3 ligases ubiquitylate ADP-ribosyl modification on nucleic acids. *Nucleic Acids Res* **52**, 801–815.

51 Nagano Y, Yamashita H, Takahashi T, Kishida S, Nakamura T, Iseki E, Hattori N, Mizuno Y, Kikuchi A & Matsumoto M (2003) Siah-1 Facilitates Ubiquitination and Degradation of Synphilin-1*. *J Biol Chem* **278**, 51504–51514.

52 Szargel R, Rott R, Eyal A, Haskin J, Shani V, Balan L, Wolosker H & Engelender S (2009) Synphilin-1A Inhibits Seven in Absentia Homolog (SIAH) and Modulates α-Synuclein Monoubiquitylation and Inclusion Formation *. *J Biol Chem* **284**, 11706–11716.

53 Eyal A, Szargel R, Avraham E, Liani E, Haskin J, Rott R & Engelender S (2006) Synphilin-1A: An aggregation-prone isoform of synphilin-1 that causes neuronal death and is present in aggregates from α-synucleinopathy patients. *Proc Natl Acad Sci* **103**, 5917–5922.

54 Ma Y, Ding L, Li Z & Zhou C (2023) Structural basis for TRIM72 oligomerization during membrane damage repair. *Nat Commun* **14**, 1555.

55 Park SH, Han J, Jeong B-C, Song JH, Jang SH, Jeong H, Kim BH, Ko Y-G, Park Z-Y, Lee KE, Hyun J & Song HK (2023) Structure and activation of the RING E3 ubiquitin ligase TRIM72 on the membrane. *Nat Struct Mol Biol* **30**, 1695–1706.

56 Mance L, Bigot N, Sánchez EZ, Coste F, Martín-González N, Zentout S, Biliškov M, Pukało Z, Mishra A, Chapuis C, Arteni A-A, Lateur A, Goffinont S, Gaudon V, Talhaoui I, Casuso I, Beaufour M, Garnier N, Artzner F, Cadene M, Huet S, Castaing B & Suskiewicz MJ (2024) Dynamic BTB-domain filaments promote clustering of ZBTB proteins. *Mol Cell* **84**, 2490-2510.e9.

57 Kim CA, Phillips ML, Kim W, Gingery M, Tran HH, Robinson MA, Faham S & Bowie JU (2001) Polymerization of the SAM domain of TEL in leukemogenesis and transcriptional repression. *EMBO J* **20**, 4173–4182.

58 Thul PJ, Åkesson L, Wiking M, Mahdessian D, Geladaki A, Ait Blal H, Alm T, Asplund A, Björk L, Breckels LM, Bäckström A, Danielsson F, Fagerberg L, Fall J, Gatto L, Gnann C, Hober S, Hjelmare M, Johansson F, Lee S, Lindskog C, Mulder J, Mulvey CM, Nilsson P, Oksvold P, Rockberg J, Schutten R, Schwenk JM, Sivertsson Å, Sjöstedt E, Skogs M, Stadler C, Sullivan DP, Tegel H, Winsnes C, Zhang C, Zwahlen M, Mardinoglu A, Pontén F, von Feilitzen K, Lilley KS, Uhlén M & Lundberg E (2017) A subcellular map of the human proteome. *Science* **356**, eaal3321.

59 Pierce WK, Grace CR, Lee J, Nourse A, Marzahn MR, Watson ER, High AA, Peng J, Schulman BA & Mittag T (2016) Multiple Weak Linear Motifs Enhance Recruitment and Processivity in SPOP-Mediated Substrate Ubiquitination. *J Mol Biol* **428**, 1256–1271.

60 De Rycker M & Price CM (2004) Tankyrase polymerization is controlled by its sterile alpha motif and poly (ADP-ribose) polymerase domains. *Mol Cell Biol* **24**, 9802–9812.

61 Mariotti L, Templeton CM, Ranes M, Paracuellos P, Cronin N, Beuron F, Morris E & Guettler S (2016) Tankyrase requires SAM domain-dependent polymerization to support Wnt-β-catenin signaling. *Mol Cell* **63**, 498–513.

62 Riccio AA, McCauley M, Langelier M-F & Pascal JM (2016) Tankyrase sterile α motif domain polymerization is required for its role in Wnt signaling. *Structure* **24**, 1573–1581.

63 Pillay N, Mariotti L, Zaleska M, Inian O, Jessop M, Hibbs S, Desfosses A, Hopkins PC, Templeton CM & Beuron F (2022) Structural basis of tankyrase activation by polymerization. *Nature* **612**, 162–169.

64 Morrone S, Cheng Z, Moon RT, Cong F & Xu W (2012) Crystal structure of a Tankyrase-Axin complex and its implications for Axin turnover and Tankyrase substrate recruitment. *Proc Natl Acad Sci U S A* **109**, 1500–1505.

65 Kabsch W (2010) XDS. *Acta Crystallogr D Biol Crystallogr* **66**, 125–132.

66 Evans PR & Murshudov GN (2013) How good are my data and what is the resolution? *Acta Crystallogr D Biol Crystallogr* **69**, 1204–1214.

67 McCoy AJ (2007) Solving structures of protein complexes by molecular replacement with Phaser. *Acta Crystallogr D Biol Crystallogr* **63**, 32–41.

68 Adams PD, Afonine PV, Bunkóczi G, Chen VB, Davis IW, Echols N, Headd JJ, Hung L-W, Kapral GJ, Grosse-Kunstleve RW, McCoy AJ, Moriarty NW, Oeffner R, Read RJ, Richardson DC, Richardson JS, Terwilliger TC & Zwart PH (2010) PHENIX: a comprehensive Python-based system for macromolecular structure solution. *Acta Crystallogr D Biol Crystallogr* **66**, 213–221.

69 Emsley P & Cowtan K (2004) Coot: model-building tools for molecular graphics. *Acta Crystallogr D Biol Crystallogr* **60**, 2126–2132.

70 Davis IW, Leaver-Fay A, Chen VB, Block JN, Kapral GJ, Wang X, Murray LW, Arendall WB, Snoeyink J, Richardson JS & Richardson DC (2007) MolProbity: all-atom contacts and structure validation for proteins and nucleic acids. *Nucleic Acids Res* **35**, W375-383.

71 DeLano WL (2002) Pymol: An open-source molecular graphics tool. *CCP4 Newsl Protein Crystallogr* **40**.

72 Pettersen EF, Goddard TD, Huang CC, Couch GS, Greenblatt DM, Meng EC & Ferrin TE (2004) UCSF Chimera—A visualization system for exploratory research and analysis. *J Comput Chem* **25**, 1605–1612.

73 Sievers F, Wilm A, Dineen D, Gibson TJ, Karplus K, Li W, Lopez R, McWilliam H, Remmert M, Söding J, Thompson JD & Higgins DG (2011) Fast, scalable generation of high-quality protein multiple sequence alignments using Clustal Omega. *Mol Syst Biol* **7**, 539.

74 The UniProt Consortium (2023) UniProt: the Universal Protein Knowledgebase in 2023. *Nucleic Acids Res* **51**, D523–D531.

75 Robert X & Gouet P (2014) Deciphering key features in protein structures with the new ENDscript server. *Nucleic Acids Res* **42**, W320–W324.

76 Mirdita M, Schütze K, Moriwaki Y, Heo L, Ovchinnikov S & Steinegger M (2022) ColabFold: making protein folding accessible to all. *Nat Methods*, 1–4.

77 Steinegger M & Söding J (2017) MMseqs2 enables sensitive protein sequence searching for the analysis of massive data sets. *Nat Biotechnol* **35**, 1026–1028.

78 Jumper J, Evans R, Pritzel A, Green T, Figurnov M, Ronneberger O, Tunyasuvunakool K, Bates R, Žídek A & Potapenko A (2021) Highly accurate protein structure prediction with AlphaFold. *Nature* **596**, 583–589.

79 Zhang Y & Skolnick J (2004) Scoring function for automated assessment of protein structure template quality. *Proteins Struct Funct Bioinforma* **57**, 702–710.

80 Yin R, Feng BY, Varshney A & Pierce BG (2022) Benchmarking AlphaFold for protein complex modeling reveals accuracy determinants. *Protein Sci* **31**, e4379.

81 Bolte S & Cordelières FP (2006) A guided tour into subcellular colocalization analysis in light microscopy. *J Microsc* **224**, 213–232.

82 Zhu K, Suskiewicz MJ, Hloušek-Kasun A, Meudal H, Mikoč A, Aucagne V, Ahel D & Ahel I (2022) DELTEX E3 ligases ubiquitylate ADP-ribosyl modification on protein substrates. *Sci Adv* **8**, eadd4253.

Materials and methods

Protein production and purification

pET-21a(+) plasmids encoding polypeptides composed of a start methionine, various indicated fragments of human SIAH1 (UniProt ID: **Q8IUQ4**), and a noncleavable -LEHHHHHH C-terminal tag were prepared through DNA synthesis of codon-optimised insert sequences (without a stop codon) and their subsequent cloning using NdeI and XhoI restriction sites. The tested SIAH1 fragments included a full-length construct as well as truncated forms encompassing residues 28-100, 28-125, or 28-157. The plasmid encoding the V90R mutant of the 28-125 fragment of SIAH1 was created using a standard site-directed polymerase chain reaction (PCR) mutagenesis protocol.

Protein production was performed overnight at 18 °C in BL21 (DE3) *Escherichia coli* cells grown in Luria-Bertani/lysogeny broth (LB) medium supplemented with 50 µg/ml ampicillin. The culture was first grown at 37 °C until the optical density at 600 nm reached 0.8, when the temperature was lowered to 18 °C and the expression induced with 0.5 mM isopropyl β- d-1-thiogalactopyranoside (IPTG).

The 28-125 fragment, assessed as the most promising fragment after initial protein production tests, was produced in 4 litres of LB culture, harvested by centrifugation (10 min at 4,000 g), incubated in a buffer 25 mM 4-(2-hydroxyethyl)-1-piperazineethanesulfonic acid (HEPES), pH 7.5, 500 mM NaCl, and 0.5 mM tris(2-carboxyethyl)phosphine (TCEP) supplemented with lysozyme (0.5 mg/ml) and benzonase (15 U/ml) for 1 h at room temperature, sonicated, and cleared by centrifugation (30 min at 12,000 g). The protein was purified from the supernatant through a three-step procedure involving a NiNTA HisTrap FF column, a HiTrapQ ion-exchange column, and a 16/60 Superdex 75 size-exclusion chromatography column (all columns from Cytiva, Marlborough, MA, USA). The NiNTA step was performed in a buffer containing 25 mM HEPES, pH 7.5, 500 mM NaCl, and 0.5 mM TCEP, with 50 mM and 250 mM imidazole added for washing and elution, respectively. The HiTrapQ step was performed in a buffer containing 25 mM HEPES, pH 7.5, 0.5 mM TCEP and between 0 and 1000 mM NaCl during the elution gradient. The final size-exclusion chromatography step was performed in a buffer containing 25 mM tris(hydroxymethyl)aminomethane (Tris), pH 7.5, 200 mM NaCl, 0.5 mM TCEP. The V90R mutant of SIAH1 28-125 was produced and purified in the same way as the WT protein. A part of the V90R mutant after the NiNTA step was observed to be bound to a bacterial contaminant (presumably the DnaK chaperone), but a pure fraction could be separated from the contaminated fraction as separate peaks at the HiTrapQ step. Proteins were concentrated using a centrifugal concentrator, flash-frozen in liquid nitrogen, and stored at -80 °C.

Protein crystallisation

We carried out crystallisation using the purified SIAH1 fragment (28-125) at 40 mg/ml in the final size-exclusion chromatography buffer (25 mM Tris, pH 7.5, 200 mM NaCl, 0.5 mM TCEP). Crystallisation trials were performed in drops containing 100 nl reservoir and 100 nl using the sitting-drop vapour-diffusion method at 20 °C. The drops were pipetted using a Mosquito liquid handling instrument (STP LabTech, Melbourn, UK) with the following initial screens from Molecular Dimension, Roterham, UK: Morpheus I, MIDASplus, ProPlex, Structure Screen Combination, and Wizard Classic 1 and 2. Best diffracting crystals were observed in the condition 1.37 of the Morpheus I screen (0.1 M MES-imidazole buffer pH 6.5, 30 % PEG550MME-20K, 0.02 M each of the alcohols 1,6-hexanediol, 1-butanol, 1,2-propanediol, 2-propanol, 1,4-butanediol, 1,3-propanediol) and were flash-frozen without addition of a cryoprotectant.

X-ray diffraction data collection and protein structure determination

100 K X-ray diffraction data were collected remotely on the PROXIMA-1 beamline at the SOLEIL synchrotron. The data were processed using XDS [65] and AIMLESS [66]. Molecular replacement using an AlphaFold model of the crystallised sequence was performed with Phaser [67] of the Phenix suite [68]. The atomic model was rebuilt in COOT [69] and refined using phenix.refine. The final R_{free} and R_{work} values were 20.38% and 23.68%, respectively (see **Table 1** for these and other statistics). The final model was validated with MolProbity [70]. Molecular graphic images were created using PyMol [71] (Schrödinger, Inc., New York, NY, USA) and UCSF Chimera [72].

Analytical size-exclusion chromatography coupled with right- and small-angle laser light scattering (SEC-RALS/LALS)

The average molecular weight of WT and V90R mutant of SIAH1 RING-ZnF1 fragments were determined by SEC-RALS/LALS in a similar manner as described before [56] using an Agilent 1260 Infinity HPLC system (Agilent, Santa Clara, CA, USA) with a diode array detector connected in line with a laser light-scattering and a differential refractometer. Light-scattering measurements were taken at two angles (15 and 90°). For each sample, we prepared 10 µL at the protein concentration indicated in the figure legend (**Figure 2A**) or within the figure itself (**Figure 3G**). The samples were injected, using an automatic sample loader, onto an Agilent AdvanceBio SEC 300A column (2.7 µm, 7.8 x 300 mm) pre-equilibrated at least overnight with 1X PBS buffer filtered three times. Column temperature was set to 30 °C, and the flow rate to 1 ml/min. The total run time for each sample was 18 min. Following the runs, the data were analysed using the Agilent GPC/SEC software using a refractive index increment value (dn/dc) of 0.185 ml/g for the calculation of protein molecular weights. Note that the SEC profiles in **Figures 2A** and **3G** are not directly comparable due to a slight difference in the experimental setup.

Multiple sequence and structural alignments

The multiple sequence alignment shown in Supplementary Figure 1 and Figure 2B was performed, using Clustal Omega [73], with sequences derived from UniProt [74]. The figures were created with ESPript 3.0 [75] and manually modified. Structural alignments were performed in PyMol [71] using “align” or “super” commands, with RMSD calculations performed over C_α atoms of residues from indicated regions that can be aligned on the sequence level.

AlphaFold 2 and AlphaFold 3 modelling

To model dimers of RING-ZnF1 fragments of different SINA/SIAH subfamily members, their full-length sequences were retrieved from UniProt [74] and aligned along with the sequence of our crystallised RING-ZnF1 fragment of SIAH1 using Clustal Omega [73] to identify the corresponding sequence range in each protein. The sequence fragments corresponding to the RING-ZnF1 region of each protein, identified through the alignment, were then used as inputs for modelling dimeric structural models using either the AlphaFold 3 [38] server or the ColabFold [76], a platform that predicts protein structures using MMseqs2 (Many-against-Many sequence searching) [77] along with AlphaFold 2 [37,78]. AlphaFold systems have been developed by Google DeepMind, London, UK. Both were run with default parameters. The quality of structural models was evaluated based on their pTM (predicted template modelling) [79] and ipTM (interface pTM) [80] scores ranging from 0 to 1, which assess the accuracy within chains and between chains (at the interface), respectively. The visualisation and analysis of the resulting structures was performed using PyMol [71] and UCSF Chimera software [72].

Confocal imaging

U2OS (RRID:CVCL_0042) cells were obtained from ATCC less than three years ago and have been checked for mycoplasma routinely every 3 months and additionally upon suspicion of contamination. All experiments were performed on mycoplasma-free cells. U2OS cells were seeded into eight-well Imaging Chamber CG plates (Zell-Kontakt) and transfected with plasmids indicated in figures using X-tremeGENE 360 (Sigma-Aldrich, St. Louis, MO, USA) transfection reagent according to the manufacturer's instructions over 24 hours. For proteasome inhibition, cells were treated with MG132 during 8 hours (20 µM in cell media). For live-cell experiments, growth medium was replaced with the following CO_2-independent imaging medium immediately prior to imaging: phenol red–free Leibovitz’s L-15 medium (Life Technologies, Carlsbad, CA, USA) supplemented with 20% FBS, 2 mM glutamine, penicillin (100 U/ml), and streptomycin (100 µg/ml). For immunofluorescence staining, cells were washed once with PBS before fixation with 3% paraformaldehyde for 10 min and permeabilised with 0.5% Triton X-100 in PBS for 10 min Alternatively, fixation and permeabilisation was achieved by incubating the cells with methanol at -20°C for 10 min. After washing three times with PBS, the samples were incubated in blocking buffer (3% BSA and 0.1% Triton X-100 in PBS) for 1 hour at room temperature (RT) and then incubated in primary antibody diluted in blocking buffer 1h at RT. For ubiquitin staining, we used an anti K48-ubiquitin antibody (clone Apu2 from Sigma-Aldrich) at 1/200 dilution. Microtubules were stained using an anti-alpha-tubulin from Novus, ST. Louis, MO, USA (DM1A) at 1/400 dilution. Cells were then washed twice with 0.1% Triton X-100 in PBS before incubation with fluorescently tagged secondary antibodies diluted in blocking buffer at RT for 1 hour in the dark. For actin staining, we used acti-stain 488 phalloidin (Tebu Bio, Le Perray-en-Yvelines, FR) at 1/500 dilution. Then, cells were washed twice with 0.1% Triton X-100 in PBS. Imaging was carried out on a LSM980 confocal laser scanning microscope (ZEISS, Oberkochen, DE) with a 63x/1.4-numerical aperture (N/A) oil-immersion objective lens. The fluorescence of EGFP/Alexa 488, mCherry, and Alexa 647 was excited with lasers at 488, 561, and 633 nm, respectively Pixel size was set to 73 nm. Live cells were maintained at 37 °C using a pre-heated chamber.

Image quantification

Image quantification was performed using ImageJ. For estimating the proportion of fluorescently-tagged SIAH/SINA proteins within clusters for a given cell, we first segmented these clusters using an intensity threshold equal to I_{mean}+ 3*I_{SD} where I_{mean} and I_{SD} correspond to the mean and standard deviation of the pixel intensities within the manually encircled cell, respectively. Then the background-subtracted integrated intensities within the clusters I_{clust} and for the entire cells I_{cell} were estimated to measure the fraction of fluorescence within the clusters as I_{clust}/I_{cell}. For measuring the enrichment in polyubiquitin signal at the SIAH1 clusters, the same thresholding approach was used in the SIAH1 channel using a threshold of I_{mean}+ 2*I_{SD}. The average intensities for the ubiquitin channel were measured within the clusters ($I_{ub,clust}$) and in the entire cell ($I_{ub,cell}$) and the enrichment at the clusters was estimated as $I_{ub,clust}/I_{ub,cell}$. The colocalisation between the SIAH1 and synphilin-1A channels was quantified with the Pearson coefficient using the JACoP plugin [81].

Statistics and reproducibility

Boxplots were obtained using R software (https://www.r-project.org/) with the limits corresponding to the 25th and 75th percentiles and the central line indicating the median value. The whiskers extend 1.5 times the interquartile range. Boxplots are from a characteristic experiment among at least three independent repeats. *P* values were calculated using a two-sided Student's t test, assuming unequal variances.

In-vitro ubiquitylation assay

The reactions were performed in a buffer containing 10 mM HEPES pH 7.5 and 50 mM NaCl. Each reaction contained protein components at the following concentrations: 20 µM ubiquitin (R&D Systems, cat. no. U-100H-10M), 0.5 µM E1 UBA1 (R&D Systems, cat. no. E-304-050), 4 µM E2 UBE2D1 (R&D Systems, cat. no. E2-616-100), and 4 µM of DTX3L RING-DTC (purified previously [82] and used as a positive control), SIAH1 RING-ZnF1 WT, or SIAH1 RING-ZnF1 V90R. The reactions were supplemented with 1 mM DTT, 1 mM ATP, and 5 mM $MgCl_2$ in a final reaction volume of 20 µL. After incubation at 37°C for 1 h, the reactions were stopped by the addition of a 4x sample buffer and incubation at 95°C for 5 min. The samples were analysed by sodium dodecyl sulphate (SDS)-polyacrylamide gel electrophoresis (SDS-PAGE) followed by semi-dry electrotransfer onto a polyvinylidene difluoride (PVDF) membrane, previously activated with pure methanol. The membrane was incubated in 5% w/v nonfat dry milk in Tris-buffered saline (TBS-T) buffer with 0.1% Tween 20 detergent, followed by incubation with anti-ubiquitin primary antibody (P4D1, BioLegend, San Diego, CA, USA, cat. no. 646301) at the dilution of 1:000 and horseradish peroxidase (HRP)-conjugated goat anti-mouse secondary antibody (Promega, Madison, WI, USA, cat. no. W4021) at 1:2500. The blots were developed by enhanced chemiluminescence (ECL) using the WesternBright HRP substrate (Advansta, San Jose, CA, USA, cat. no. K-12045-D50) and scanned using iBright 1500 system (Invitrogen, Waltham, MA, USA).

Author contributions

F.C. – crystal structure solution, SEC-RALS/LALS, figure preparation, experimental design and supervision, writing; A.M. – structural modelling, SEC-RALS/LALS, figure preparation, writing; C.C. – cloning, cell biology experiments; L.M. – in-vitro ubiquitylation assay, figure preparation, writing; Z.P. – protein purification and crystallisation, structural modelling; N.B. – cell biology experiments; S.G. – protein production; V.G. – protein production; N. G. – experimental design and supervision, writing; I.T. – experimental design and supervision, writing; B.C. – experimental design and supervision, writing; S.H. – experimental design and supervision, cell biology experiments, quantification, figure preparation, writing; M.J.S. – experimental design and supervision, cloning, protein purification and crystallisation, figure preparation, writing.

Acknowledgements

We thank Ivan Ahel, Gwenaël Rabut, Aurélien Bidaud-Meynard, and Grégoire Michaux for sharing reagents. We thank the French Infrastructure for Integrated Structural Biology (FRISBI), supported by the French National Research Agency (ANR) (ANR-10-INBS-0005) and the Infrastructures en Biologie Santé et Agronomie (IBISA) for support in accessing scientific infrastructure. We acknowledge the SOLEIL synchrotron and thank Pierre Legrand and Andrew Thompson for assistance at beamline PROXIMA 1. We thank Microscopy-Rennes Imaging Center (BIOSIT, Univ Rennes 1), a member of France-BioImaging supported by the ANR (grant no ANR-10-INBS-0004), for access to optical microscopy and Stéphanie Dutertre, Xavier Pinson and Gilles Le Marchand for their assistance. L.M.'s PhD stipend is financed by the Region Centre-Val de Loire and administered by Université d'Orléans. M.J.S. and his team are supported by the European Research Council (Starting Grant 'SUMOwriteNread', grant no 101078837) and the CNRS. M.J.S. is an associated fellow of Le Studium and ATIP-Avenir. This work was partially funded by the European Union; views and opinions expressed are, however, those of the author only and do not necessarily reflect those of the European Union or the European Research Council Executive Agency, who cannot be held responsible for them.

Data availability

The atomic coordinates and structure factors for human SIAH1 RING-ZnF1 have been deposited in the Protein Data Bank (PDB) under the accession code **9G0L**. All other raw data are included in this study or available from corresponding authors.

Tables

Table 1 | X-ray data collection and refinement statistics

Data collection statistics	
Radiation source	SOLEIL PROXIMA 1
Wavelength (Å)	0.97856
Spacegroup	$P4_32_12$
cell dimensions: *a, b, c* (Å)	69.85, 69.85, 62.71
α, β, γ (°)	90.00, 90.00, 90.00
Number of molecules/asymmetric unit	1
Resolution range (Å)	46.66-1.90 (1.94-1.90)
Total observations	320489 (21927)
Unique reflections	12780 (804)
Completeness (%)	100.0 (100.0)
Multiplicity	25.1 (27.3)
R_{merge} [a] (%)	10.4 (290.9)
Average *I/σ(I)*	17.0 (1.3)
$CC_{1/2}$ (%)	99.9 (66.9)
Resolution range (Å)	46.66-1.90
Number of reflections used	12728
R_{work} [b] / R_{free} [c] (%)	20.38/23.68
Average B values (Å^2)	
All atoms	50.64
Protein chain A atoms	50.73
Zinc atoms	48.78
Water atoms	49.86
Root mean square deviation from ideality	
Bond lengths (Å)	0.008
Bond angles (°)	1.041
Ramachandran analysis	
Favoured regions / Allowed regions / Outliers (% of residues)	97.9/2.1/0.0
Number of atoms	
Protein chain A	732
Zinc	3
Water	72
PDB code	**9G0L**

[a] $R_{merge} = \sum_h \sum_i |I_{h,i} - \langle I \rangle_h| / \sum_h \sum_i I_{h,i}$ where $\langle I \rangle_h$ is the mean intensity of the symmetry-equivalent reflections.
[b] $R_{work} = \sum_h ||F_o| - |F_c|| / \sum_h |F_o|$, where F_o and F_c are the observed and calculated structure factor amplitudes, respectively, for reflection h.
[c] R_{free} is the *R* value for a subset of 5% of the reflection data, which were not included in the crystallographic refinement.

Table 2 | PISA server analysis of RING:RING and SBD:SBD homodimerisation interfaces

For the SIAH1 SBD dimer, two different indicated crystal structures were analysed.

	TRIM32$^{RING:RING}$ (stable dimer)	**TRIM23$^{RING:RING}$ (transient dimer)**	**SIAH1$^{RING:RING}$**	**SIAH1$^{SBD:SBD}$**	
PDB code	**5FEY**	**5FER**	**9G0L** (this study)	**4CA1**	**4C9Z**
Interface area, Å^2	1000.3	1008.7	791.3	974.0	1105.9
Δ^iG, kcal/mol*	-14.7	-10.1	-13.7	-1.2	-1.0
N_{HB}**	9	15	6	22	21
N_{SB}***	2	0	0	12	18

* Δ^iG indicates the solvation free energy gain upon formation of the interface. Negative Δ^iG corresponds to favourable burying of hydrophobic residues.
** N_{HB} indicates the number of potential hydrogen bonds across the interface. Each hydrogen bond contributes about 0.5 kcal/mol to the free energy of protein binding.
*** N_{SB} indicates the number of potential salt bridges across the interface. Each salt bridge contributes about 0.3 kcal/mol to the free energy of protein binding

Supplementary figures

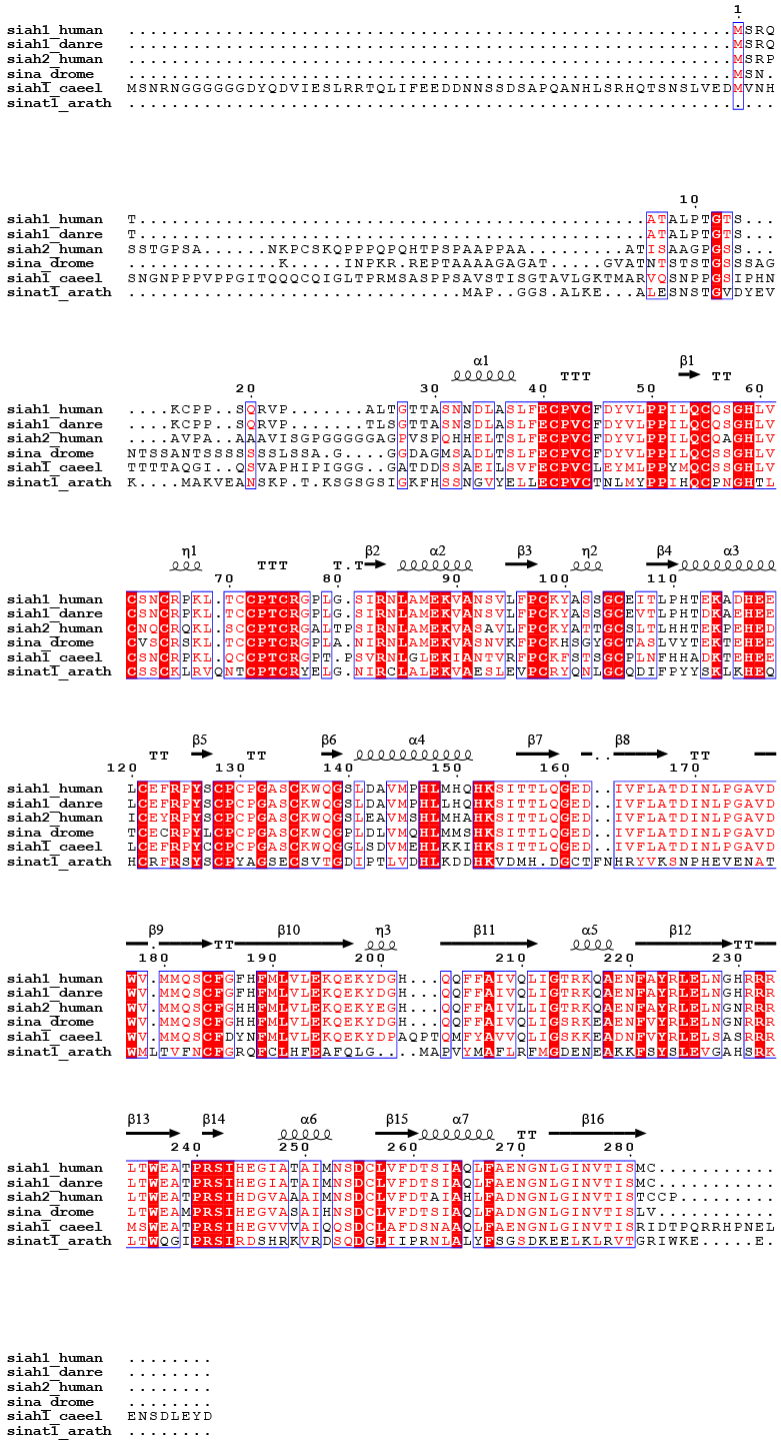

Supplementary Figure 1 | Multiple sequence alignment of selected SINA/SIAH proteins. The multiple sequence alignment was prepared in Clustal Omega and reprocessed using ESPript 3.0, with secondary structure annotated according to the AlphaFold 2 model of human SIAH1. Analysed sequences include SIAH1 and SIAH2 from *H. sapiens* (siah1_human, UniProt ID: **Q8IUQ4** and siah2_human, UniProt ID: **O43255**), SIAH1 from *D. rerio* (siah1_danre, UniProt ID: **Q7ZVG6**), SINA from *D. melanogaster* (sina_drome, UniProt ID**: P21461**), SIAH1 from *C. elegans* (siah1_caeel, UniProt ID: **Q965X6**), and SINAT1 from *A. thaliana* (sinat1_arath, UniProt ID: **P93748**). Helices *α1* and *α2* correspond to the RING extensions shown in Figure 2B.

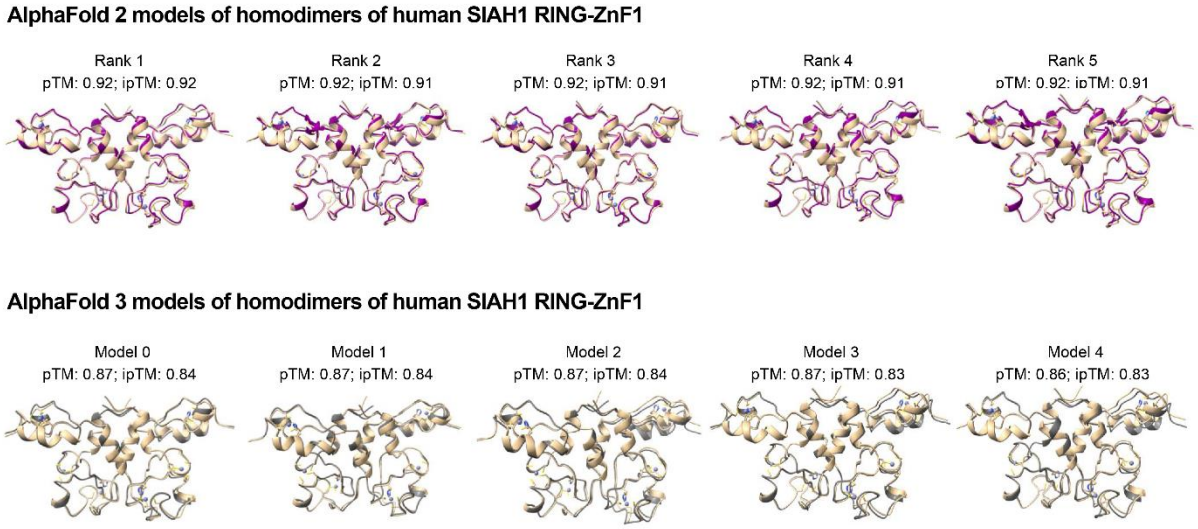

Supplementary Figure 2 | AlphaFold models of SIAH1 RING-ZnF1 dimerisation. Ribbon diagrams showing structural superposition between the crystallographic dimer of the RING-ZnF1 fragment of human SIAH1 (light pink) and either AlphaFold 2 (purple) or AlphaFold 3 (grey) models of that dimer. All five models generated with each programme are provided together with confidence metrics: pTM (predicted template modelling score) and ipTM (interface predicted template modelling score). Structural figures were created in Chimera.

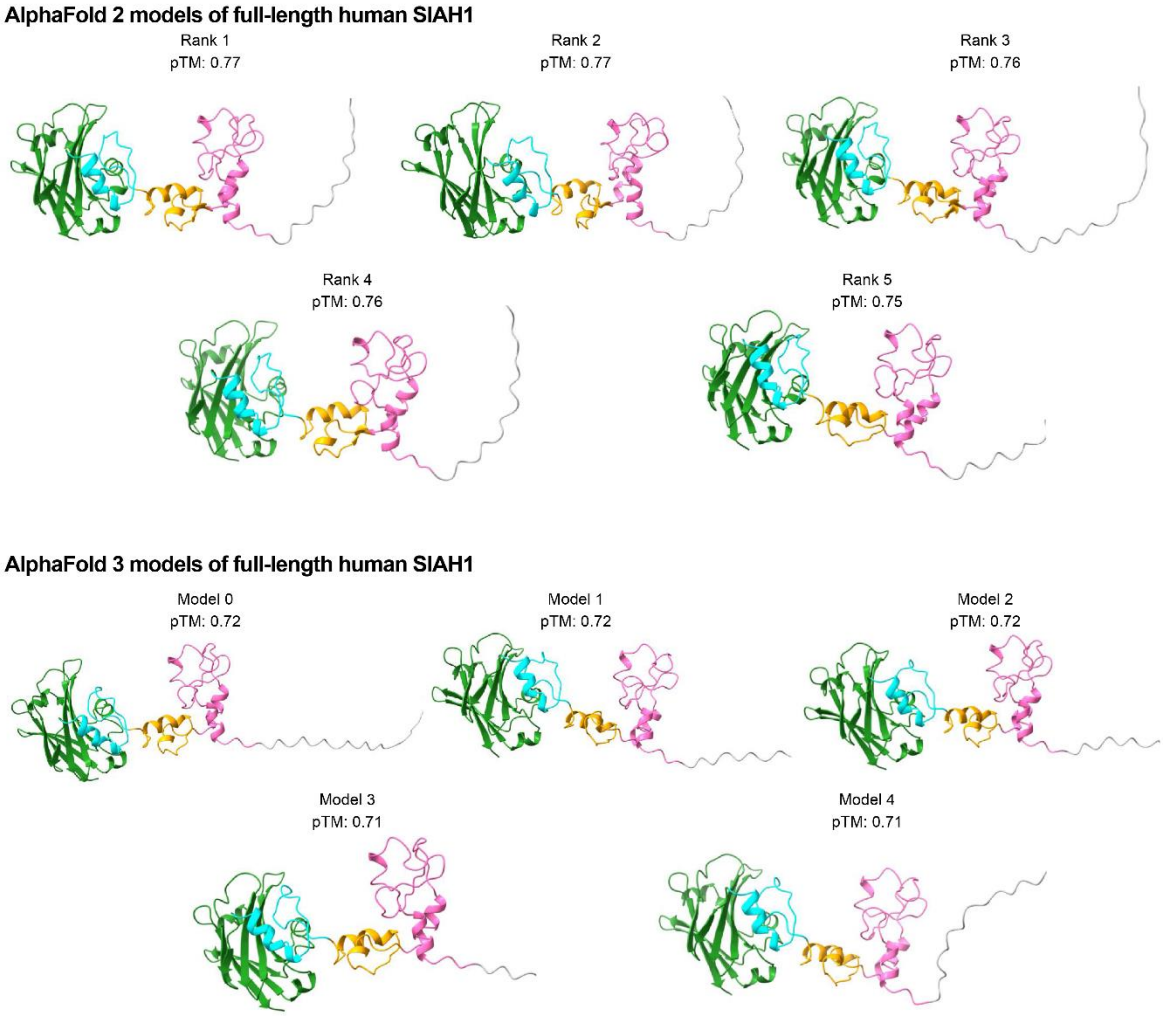

Supplementary Figure 3 | AlphaFold models of full-length SIAH1. Ribbon diagram of AlphaFold 2 and AlphaFold 3 models of full-length human SIAH1. SIAH1 is coloured according to domain composition like in Figure 1A. All five models generated with each programme are provided together with their pTM (predicted template modelling) score. Structural figures were created in Chimera.

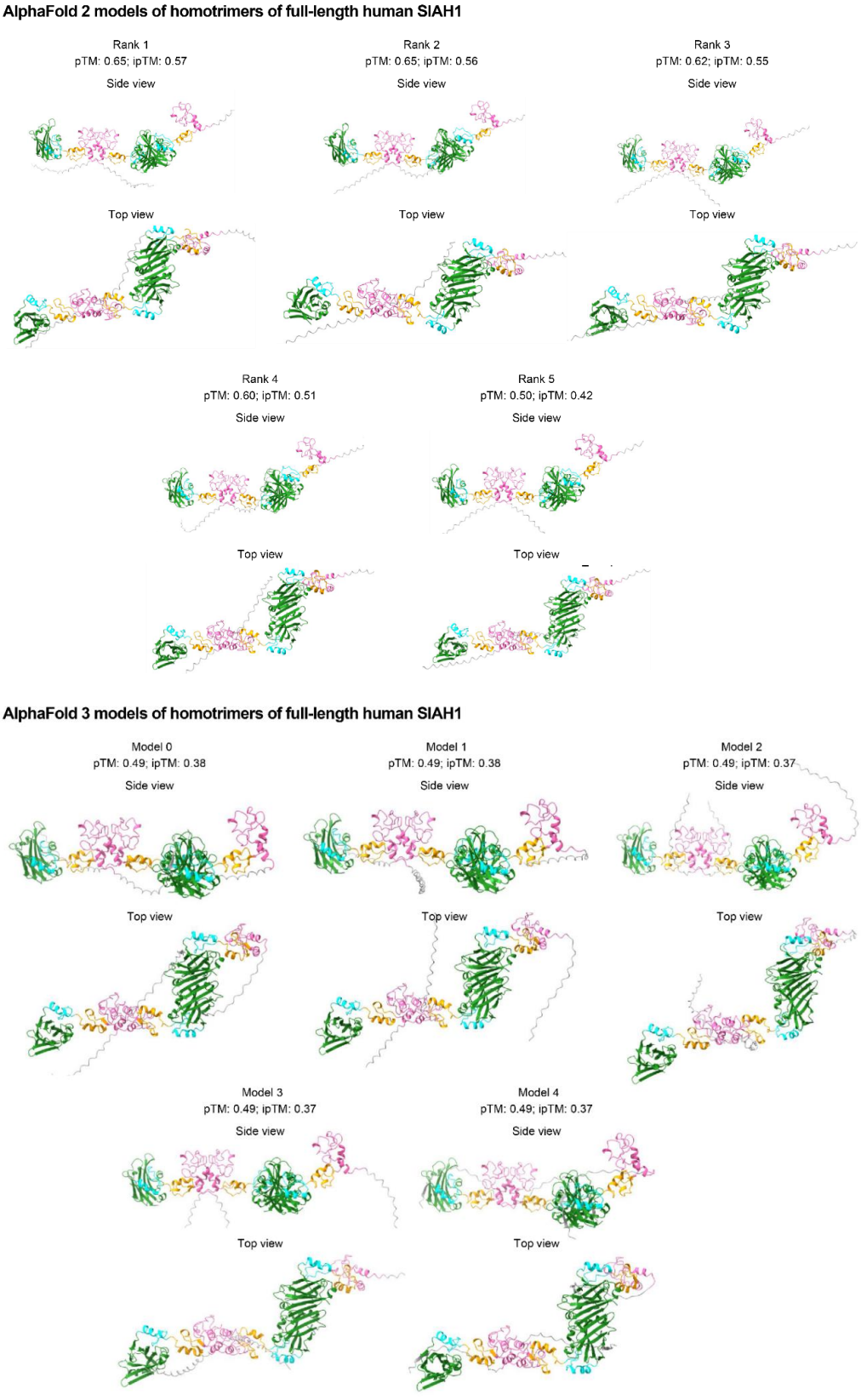

Supplementary Figure 4 | AlphaFold models of full-length SIAH1 trimers. Ribbon diagram of AlphaFold 2 and AlphaFold 3 models of a trimer of full-length human SIAH1. Each SIAH1 subunit is coloured according to domain composition like in Figure 1A. All five models generated with each programme are provided together with confidence metrics: pTM (predicted template modelling score) and ipTM (interface predicted template modelling score). Structural figures were created in Chimera.

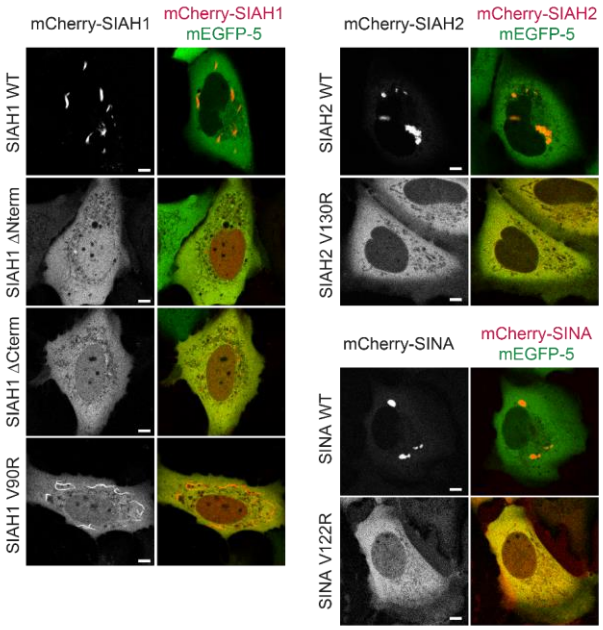

Supplementary Figure 5 | Subcellular localisation analysis of SINA/SIAH proteins. An additional set of representative confocal images of live cells expressing WT or mutant variants of mCherry-tagged SINA/SIAH proteins to accompany Figure 4B, D, and F. In the merged image, colocalisation with an mEGFP-5 (composed of five fused EGFP proteins) control is shown. All scale bars in cell images correspond to 5 µm.